University of Essex

Research Repository

A hierarchical graph learning framework for VR-based motor imagery decoding driven by MVMD and feature optimization

Accepted for publication in the Journal of Neural Engineering

Research Repository link: https://repository.essex.ac.uk/43919/

Please note:

Changes made as a result of publishing processes such as copy-editing, formatting and page numbers may not be reflected in this version. For the definitive version of this publication, please refer to the published source. You are advised to consult the published version if you wish to cite this paper.
https://doi.org/10.1088/1741-2552/aeabf5

www.essex.ac.uk

University of Essex

A Hierarchical Graph Learning Framework for VR-Based Motor Imagery Decoding Driven by MVMD and Feature Optimization

Kaiyue Du[1], Wenwen Chang[1,2,*], Weixuan Kong[1], He Huang[1], Guanghui Yan[1] and Muhammad Tariq Sadiq[3]

[1] School of Electronic and Information Engineering, Lanzhou Jiaotong University, Lanzhou, 730070 China.
[2] Postdoctoral Innovation Practice Base, Lanzhou Beike Weituo Technology Co., Ltd., Lanzhou, China.
[3] School of Computer Science and Electronic Engineering, University of Essex, Colchester CO4 3SQ, U.K.

*Author to whom any correspondence should be addressed.

E-mail: changww2013@126.com

Keywords: Motor Imagery, Virtual Reality, Multivariate Variational Mode Decomposition, Graph Convolutional Networks, Brain Network Analysis, Neurorehabilitation

Abstract

Objective. While virtual reality (VR) combined with action observation (AO) provides enriched visual guidance for motor imagery (MI), the decoding stability of MI Brain–Computer Interface (BCI) remains a challenge due to the inherent non-stationarity and low signal-to-noise ratio of Electroencephalography (EEG) signals in dynamic environments. Enhancing decoding accuracy and understanding neural representations in VR-based AO+MI tasks remain important challenges in neural engineering. *Approach.* This study proposes a hierarchical graph learning framework tailored for VR-based MI decoding, leveraging multivariate variational mode decomposition (MVMD) to decouple complex EEG signals into rhythmic components for enhanced multi-domain feature analysis, hybrid feature selection for compact representation, and functional brain network modeling based on phase locking value. Each EEG trial is represented as a sparsified graph, and a hierarchical graph convolutional network is designed to capture multi-scale spatial dependencies and high-order interactions for classification. *Main results*. Experimental evaluations on a lab-acquired VR-MI dataset demonstrate that the proposed framework achieves competitive three-class decoding accuracy. This performance surpasses baseline models such as EEGNet, as observed under VR-based motor imagery conditions. In addition to enhanced decoding performance, the study enables neurophysiological interpretation by characterizing VR-induced modulations in brain network organization. *Significance*. VR-based AO+MI paradigm is found to enhance sensorimotor connectivity and promote large-scale network integration, indicating more coordinated neural dynamics during MI tasks. These findings suggest that the proposed framework effectively improves VR-based AO+MI decoding while providing interpretable insights into neural mechanisms, supporting its potential for advanced BCI applications.

1. Introduction

Brain-computer interface (BCI) systems establish a direct communication pathway between neural activity and external devices, bypassing conventional neuromuscular channels. Among various BCI paradigms, Motor Imagery (MI)-based BCI has attracted extensive attention because it enables users to generate controllable neural patterns without physical movement, showing considerable potential in rehabilitation, assistive communication, and human-machine interaction [1-3].

Neurophysiologically, MI induces task-related modulation of sensorimotor rhythms, particularly in the μ (8–13 Hz) and β (13–30 Hz) bands, which are commonly characterized by event-related desynchronization (ERD). These EEG signatures provide important biomarkers for MI-BCI decoding and neural rehabilitation[4-5].

Despite its considerable potential, the practical application of MI-BCI continues to face significant challenges. Due to the low signal-to-noise ratio (SNR) and non-stationary characteristics of EEG data, accurate classification of different types of MI-EEG signals remains highly challenging [2].Implementing EEG-based BCI systems for Motor Imagery recognition in real-world application scenarios is hindered primarily by inherent inter-individual variability and the low SNR of EEG signals [6]. Recently, VR-assisted MI paradigms have emerged as a promising approach to improve user engagement and provide immersive feedback. However, the neural mechanisms underlying VR-induced modulation of MI representations remain insufficiently understood [4]. Nevertheless, how to systematically elucidate the influence of VR on the neural representations of MI from both the signal decoding and neuromechanistic perspectives remains a critical scientific question that urgently requires investigation. Addressing the challenges of enhanced EEG non-stationarity, complex cross-regional neural interactions, and limited decoding stability in virtual reality-based motor imagery (VR-MI), this study presents an integrated decoding framework and a paired MI/VR-MI experimental dataset. The main contributions are summarized as follows:

(1) A paired MI/VR-MI EEG dataset is established using a conventional cue-based MI paradigm and a VR-based action observation plus MI paradigm. This dataset provides a valuable resource for investigating EEG decoding and neural differences between MI paradigms, where public VR-MI datasets remain limited.

(2) An integrated decoding framework combining MVMD, multi-domain feature extraction, feature optimization, and hierarchical graph learning is developed. By integrating complementary signal processing and graph learning strategies, the framework improves EEG representation and functional interaction modeling.

(3) The proposed framework incorporates PLV-based functional connectivity into hierarchical graph learning to capture multi-scale spatial dependencies and higher-order brain interactions, achieving competitive decoding performance on three-class MI tasks.

(4) Comparative experiments on the paired dataset demonstrate the effectiveness of the proposed framework and provide evidence for differences in decoding performance, functional connectivity, and EEG feature representations between conventional MI and VR-based action observation plus MI paradigms.

2. Related work

The traditional technical pipeline for MI-EEG decoding relies on the combination of manually engineered features with shallow classifiers, such as Common Spatial Pattern (CSP) coupled with Support Vector Machine (SVM) or Linear Discriminant Analysis (LDA) [7].To achieve effective sub-band representation, earlier works integrated dual-tree complex wavelet filter banks with the Common Spatial Pattern (CSP) algorithm for the purpose of hierarchical signal breakdown and subsequent spatial profiling [8]. Although these methods achieve satisfactory performance under specific conditions, their dependence on manually designed features limits their ability to characterize the complex spatial–temporal patterns of non-stationary EEG signals.

Recent advances in deep learning have significantly improved MI-EEG decoding by enabling automatic feature learning from raw EEG signals [9]. Convolutional Neural Networks (CNNs) have demonstrated strong capability in extracting local spatial and temporal features. Representative studies include EEG Conformer [10-11], which combines convolutional feature extraction with Transformer-based global dependency modeling, ATCNet [12], which incorporates domain-specific priors into temporal convolutional networks, and EEG-Deformer[13], which integrates dense convolutional connections with Transformer architectures. Recurrent neural-network approaches have also been proposed to model spatial and temporal dependencies in MI-EEG [14]. Despite these advances, CNN-based methods mainly operate in Euclidean space and therefore cannot explicitly model the complex topological relationships among EEG channels, limiting their ability to characterize large-scale functional interactions in the brain.

To better characterize the non-stationary oscillatory properties of multi-channel EEG signals, Multivariate Variational Mode Decomposition (MVMD) has recently attracted increasing attention. As a multichannel extension of Variational Mode Decomposition (VMD), MVMD simultaneously

decomposes all EEG channels into frequency-aligned intrinsic mode functions, providing superior consistency across channels and improved robustness for multivariate neural signal analysis [15].

Several studies have demonstrated the effectiveness of MVMD for MI-EEG decoding. Sadiq et al. [16] first introduced MVMD into MI classification and reported substantial improvements over MEMD-, MSWT-, and MEWT-based methods by combining MVMD with ReliefF feature selection. Jian et al. [17] further proposed grouped multivariate variational mode decomposition for EEG analysis. Nevertheless, existing MVMD-based approaches mainly employ conventional statistical or nonlinear feature extraction after signal decomposition. The potential of integrating MVMD-derived multi-scale neural representations with graph-based deep learning frameworks has not yet been fully explored.

To overcome the limitations of Euclidean feature learning, Graph Convolutional Networks (GCNs) have been increasingly adopted for EEG decoding because they naturally model non-Euclidean topological relationships among electrodes [18]. Existing studies have explored various graph construction strategies. Hou et al.[47] proposed GCNs-Net based on Pearson correlation-derived graph Laplacians. Dense-GCN [19] integrates dense graph convolutions with enhanced S-transform features to jointly capture temporal, spectral, and spatial information. More recently, LGGNet [20] introduced hierarchical graph learning based on functional brain partitions, whereas MGCANet [21] fused multiple anatomical and functional brain graphs using adaptive attention mechanisms. Xue et al. [18] proposed F-FGCN by constructing functional graphs from Pearson correlation matrices and achieved competitive decoding performance on the PhysioNet dataset.

Although these methods effectively exploit graph topology, most rely on a single graph representation and rarely consider the interaction between multi-scale signal decomposition and graph representation learning. Consequently, the complementary advantages of frequency-aligned neural representations and functional brain topology remain insufficiently utilized.

Recently, VR has been increasingly integrated into MI-BCI systems to provide immersive feedback and improve user engagement. Previous studies have demonstrated the potential of VR-based paradigms in enhancing MI performance and supporting rehabilitation-oriented applications [22-28]. However, existing VR-MI investigations mainly focus on behavioral improvements or conventional EEG biomarkers, while the influence of VR on large-scale functional brain organization, dynamic neural representations, and decoding-oriented mechanisms remains insufficiently explored.

Motivated by these gaps, this study develops a novel MVMD-FSGCN framework that integrates multi-scale feature extraction, adaptive graph construction, and hierarchical graph representation learning. Specifically, MVMD is utilized to decompose EEG signals into frequency-aligned intrinsic modes, while a node-wise hybrid feature selection strategy—integrating mRMR, ReliefF, RFE, and LASSO—is employed to extract compact and discriminative representations. To characterize dynamic brain connectivity, each EEG trial is modeled as a graph based on Phase Locking Value (PLV), complemented by an adaptive sparsification strategy using the upper quartile threshold to preserve essential functional connections while mitigating noise. A hierarchical GCN architecture with pooling is then implemented to capture both local and high-order topological interactions.

Experimental results indicate that the proposed framework outperformed the evaluated traditional and deep-learning baselines under the reported subject-specific protocol. Notably, the mean accuracy under the combined VR-based AO+MI condition was 70.30%, compared with 60.20% under conventional MI (Holm-adjusted $p = 0.006$, Cohen's $dz = 0.62$). Further analysis indicates condition-related differences in functional connectivity, with group-level graph measures showing significant Beta-band changes in global efficiency and characteristic path length. Ablation analyses further examine the contribution of decomposition, feature selection, graph construction, and hierarchical pooling. Overall, the findings support the proposed framework for subject-specific decoding and provide an interpretable comparison of the two experimental conditions.

3. Materials AND Methods

3.1. Dataset

Due to the limited availability of data sets regarding the Motor Imagery paradigm under VR conditions, we utilized a variety of EEG data sets collected by our laboratory and designed specifically

for different rehabilitation paradigms. The study was approved by the Ethics Committee of Gansu Provincial Maternity and Child-care Hospital (Gansu Provincial Central Hospital)((2023) GSFY Ethics [90]) and conducted in strict accordance with the Declaration of Helsinki. These data sets are publicly available at https://figshare.com/articles/dataset/A_Multi-Paradigm_EEG_Dataset_for_Studying_Upper_Limb_Rehabilitation_Exercises_Raw_EEG_Dataset/28831730/2.

3.1.1. Participants

A total of 30 healthy subjects (15 males and 15 females, aged 20–33 years) were initially recruited. However, two subjects (S207 and S218) were excluded prior to the analysis due to excessive artifact contamination and suboptimal signal quality. Consequently, data from the remaining 28 subjects (14 males and 14 females) were included in the final study. All participants were right-handed according to the Edinburgh Handedness Inventory [29], and had normal or corrected-to-normal vision. The study was conducted in accordance with the Declaration of Helsinki [30], and written informed consent was obtained from all participants prior to the experiment. To minimize confounding effects on cortical activity, subjects were required to maintain adequate sleep and strictly abstain from caffeine-containing beverages for at least 12 hours before data collection [31].

3.1.2. Experimental Paradigms

The experiment comprised two paradigms: a conventional Motor Imagery (MI) paradigm and a virtual reality-based motor imagery (VR-MI) paradigm.

Paradigm 1 (MI): Participants positioned their arms on the desk surface while concentrating on a central "+" symbol. Following the removal of this fixation point, they noted the specific side on which a square emerged. Depending on whether the square appeared on the left, right, or both sides, subjects imagined performing a grasping-releasing task with the corresponding hand(s) without any actual motor execution. The experimental paradigm is illustrated in Figure 1 (a).

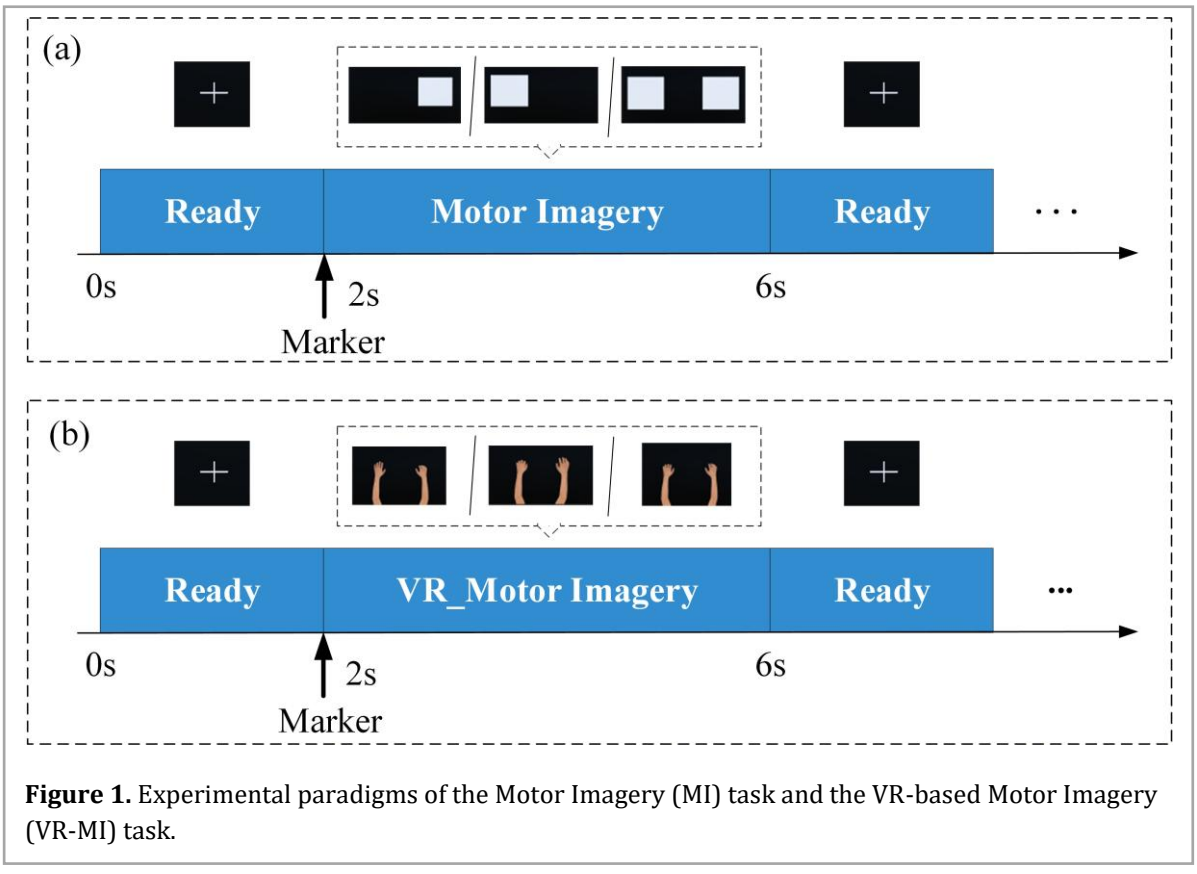


Figure 1. Experimental paradigms of the Motor Imagery (MI) task and the VR-based Motor Imagery (VR-MI) task.

Paradigm 2 (VR-based MI): Participants wore VR glasses and focused on a central "+" symbol within the VR display. In the virtual scene, participants observed the actions of virtual hands (left, right, or both) and simultaneously performed the corresponding motor imagery. The experimental paradigm is illustrated in Figure 1(b).

Each imagery task lasted for 4 s, followed by a 2 s rest period. Each experimental session lasted 3 minutes, during which 10 trials were performed for each hand. Each paradigm was repeated 4 times, ensuring that each subject accumulated a total of 40 valid trials per task.

3.1.3. Data Acquisition and Preprocessing

This study employed the NeuSen W series wireless electroencephalography acquisition system, manufactured by Neuracle Technology Co., Ltd. (China), for data acquisition. A total of 59 EEG electrodes were positioned according to the international 10–20 system [32]. The initial sampling rate was set to 1000 Hz, with electrode impedance maintained below 20 kΩ. In addition, electrooculogram (EOG) and electrocardiogram (ECG) signals were simultaneously recorded for artifact identification.

The raw data from 28 subjects were preprocessed using the EEGLAB toolbox in MATLAB as follows [33]: (1) Electrode localization was performed, and non-essential channels ('ECG', 'HEOR', 'HEOL', 'VEOU', 'VEOL') were removed; (2) Common average referencing and band-pass filtering (8-30 Hz, corresponding to motor imagery-related frequency bands) were applied [34-35]; (3) Data were downsampled from 1000 Hz to 128 Hz; (4) Bad channels were visually inspected and removed; (5) Data segmentation and merging were conducted, where 4-second task execution periods (2–6 s) from Paradigm 1 and Paradigm 2 were extracted for each subject and sequentially concatenated, followed by quality control to discard low-quality segments [36]; (6) The processed data were saved in the required format for subsequent analysis. For each subject, the final dataset included one MI recording and one VR-MI recording (e.g., for subject S201: 201MI.fdt/.set and 201VR.fdt/.set).

The final number of usable trials per class across all subjects was 37.37±6.06. It is worth noting that while the target was 40 trials, the actual counts ranged from 20 to 50. For a few subjects (e.g., S210, S202), the count exceeded 40 because additional backup blocks were recorded during the acquisition phase to compensate for potential data loss. Conversely, for subjects with higher artifact contamination (e.g., S205, S208), strict rejection criteria led to fewer remaining trials. In all cases, the trials remained approximately balanced across the three classes for each individual, with the exact per-subject trial counts provided in Table S1 of the Supplementary Material. This setup ensures that classification fairness and the reliability of the reported accuracies were not compromised by class imbalance.

3.2. VR Motor Imagery Decoding Based on the MVMD-FSGCN Framework

Based on an EEG dataset of multiple rehabilitation modalities collected in our laboratory, this paper designs an MVMD-FSGCN decoding framework. We conduct a comparative analysis of neural representations between the VR-based AO+MI paradigm and the cue-based MI paradigm, providing theoretical support for the effectiveness of a new VR-MI rehabilitation paradigm and offering critical

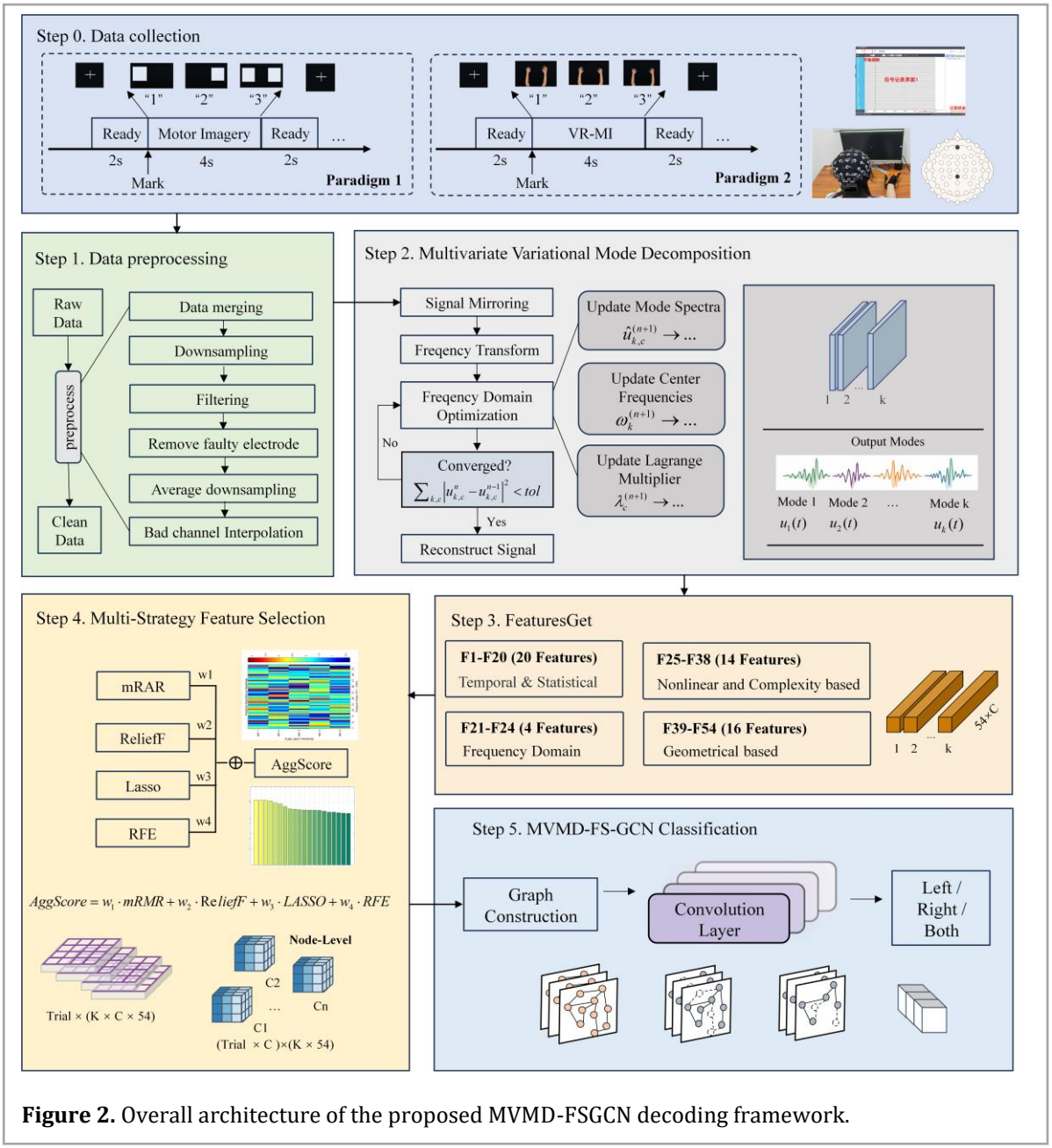


Figure 2. Overall architecture of the proposed MVMD-FSGCN decoding framework.

scientific evidence and practical guidance for developing more efficient neurorehabilitation protocols. The overall decoding framework is illustrated in Figure 2.

3.2.1. Multi-Modal Decomposition and Multi-Domain Feature Extraction

Given an EEG trial $X \in \mathbb{R}^{C\times T}$, MVMD decomposes the multichannel signal into K band-limited intrinsic modes:

$$X \to \{u_k\}_{k=1}^{K}, u_k \in \mathbb{R}^{C\times T} \tag{1}$$

The decomposition is formulated as a constrained variational problem that minimizes the sum of bandwidths of all modes while ensuring signal reconstruction:

$$\min_{\{u_k\},\{\omega_k\}} \sum_{k=1}^{K} \left\| \partial_t \left[\left(\delta(t) + \frac{j}{\pi t} \right) * u_k \cdot e^{-j\omega_k t} \right] \right\|_2^2 + \epsilon \sum_{k=1}^{K} \left\| u_k(t) \right\|_2^2 \tag{2}$$

$$\text{s.t.} \quad \sum_{k=1}^{K} u_k(t) = x(t), \quad u_k \in \mathcal{H}^1(\mathbb{R}) \tag{3}$$

In this study, MVMD is applied independently to each trial with fixed parameters, yielding a four-dimensional tensor:

$$\mathcal{U} = \left[u_k^c(t,n) \right] \in \mathbb{R}^{K \times C \times T \times N} \tag{4}$$

which preserves both channel-wise and frequency-adaptive representations.

For each decomposed mode, a 54-dimensional feature vector is extracted, including time-domain, frequency-domain, nonlinear, entropy-based, and geometric features. For each mode k and channel c, a feature vector $\mathbf{f}_{k,c} \in \mathbb{R}^{54}$ is extracted:

$$\mathbf{f}_{k,c} = \Phi(u_k^c) = \bigoplus_{d=1}^{D} \Phi_d(u_k^c) \tag{5}$$

$$\Phi_d(u) = \begin{cases} \mathbb{E}[u],\ Var(u),\ RMS(u) & d = 1 \\ \int |\hat{u}(f)|^2 \, df & d = 2 \\ \Psi(u) & d = 3 \\ \mathcal{H}(u) & d = 4 \\ \mathcal{G}(u) & d = 5 \end{cases} \tag{6}$$

Where $\Phi(\cdot)$ denotes a multi-domain feature mapping.

The extracted features include: Time-domain statistics: amplitude distribution and variability [37]; Dynamic features: first- and second-order differences, Hjorth parameters [38]; Frequency-domain features: band power in μ (8–13 Hz) and β (13–30 Hz) bands [39]; Nonlinear measures: signal energy, Teager–Kaiser energy [40]; Entropy measures: approximate entropy, sample entropy, Rényi entropy [41]; Geometric descriptors: area, centroid distance, angular variation [42]. The features are concatenated across all modes and channels:

$$F^{(i)} = vec\left(\{ f_{k,c} \}_{k=1,c=1}^{K,C} \right) \tag{7}$$

resulting in a high-dimensional representation:

$$F^{(i)} \in \mathbb{R}^{K \cdot C \cdot 54} \tag{8}$$

To further capture the morphological characteristics of EEG signals, a set of geometric features was designed by mapping the temporal waveform into geometric structures. These include area-based descriptors, centroid distances, vector lengths, angular variations, and shape-related metrics (e.g., ellipse area and octagonal approximation), providing a novel perspective on EEG signal

Table 1. Summary of Extracted Features.

Category	Feature Type	Description
Time-domain	Mean abs, RMS, variance, etc.	Amplitude statistics
Dynamic	Hjorth, FD, etc.	Temporal complexity
Frequency	Band power, etc.	Spectral energy
Nonlinear	Energy, TKEO, etc.	Nonlinear dynamics
Entropy	ApEn, SampEn, etc.	Signal irregularity
Geometric	Area, angle, centroid, etc.	Morphological features

representation. Multidimensional features are shown in Table 1. These features jointly capture amplitude, spectral, nonlinear, and morphological characteristics of EEG signals.

3.2.2. Feature Selection via Multi-Strategy Fusion

Given the high dimensionality and redundancy of the extracted features, a multi-strategy feature selection scheme is proposed to obtain a compact and discriminative representation suitable for graph-based modeling.

The original feature matrix is constructed by concatenating all modal–channel features:

$$F \in \mathbb{R}^{N\times(K\cdot C\cdot F_0)} \tag{9}$$

where N is the number of trials; K is the number of MVMD modes; C is the number of EEG channels; F_0 is the number of features per mode–channel.

To construct channel-based graph nodes, the feature tensor is reorganized along the channel dimension. Specifically, features from all MVMD modes belonging to the same EEG channel are concatenated:

$$X_{node} \in \mathbb{R}^{(N\cdot C)\times(K\cdot F_0)} \tag{10}$$

where each row corresponds to one channel node from one trial, and the feature dimension $K \cdot F_0$ represents all mode-feature combinations. The corresponding labels are expanded as:

$$Y_{node} = repeat(Y, C) \tag{11}$$

Here, the node-wise formulation is used only to organize channel-consistent feature ranking for graph construction. It does not imply that channels from the same trial are treated as independent experimental observations during data splitting or evaluation. During model evaluation, all channel nodes from the same trial are always assigned to the same cross-validation fold, ensuring that no information is shared between training and testing sets.

To obtain robust feature importance estimation, four complementary feature selection strategies are adopted, including minimum redundancy maximum relevance (mRMR) [43], ReliefF [44], LASSO [45] regression, and recursive feature elimination (RFE) [46]. For the *i*-th feature, the importance scores obtained from the four methods are denoted as:

$$S_i^{(m)}, m = 1, 2, 3, 4 \tag{12}$$

where *m* represents the feature selection strategy. For mRMR, the feature score is calculated by maximizing the relevance with class labels while minimizing redundancy among selected features:

$$S_i^{(1)} = I(f_i; y) - \frac{1}{P-1}\sum_{j\neq i} I(f_i; f_j) \tag{13}$$

where $I(\cdot)$represents mutual information, f_i is the *i*-th feature, y denotes the class label, and $P = K \times F_0$is the total number of mode-feature combinations. ReliefF evaluates feature importance according to intra-class compactness and inter-class separability:

$$S_i^{(2)} = \frac{1}{N}\sum_{n=1}^{N}\left[-\frac{1}{K_r}\sum_{h=1}^{K_r}\left\|f_i(x_n)-f_i(H_{n,h})\right\|+\frac{1}{K_r}\sum_{m=1}^{K_r}\left\|f_i(x_n)-f_i(M_{n,m})\right\|\right] \tag{14}$$

where $H_{n,h}$ and $M_{n,m}$ denote the nearest neighbors from the same and different classes, respectively, and K_r represents the number of nearest neighbors. For LASSO regression, the feature coefficients are obtained by solving:

$$\beta = \arg\min_{\beta}\left(\| y - X\beta\|_2^2 + \lambda\| \beta\|_1\right) \tag{15}$$

where λ controls the sparsity constraint. The corresponding feature importance is defined as:

$$S_i^{(3)} = | \beta_i | \tag{16}$$

For RFE, a linear SVM is iteratively trained to evaluate feature contribution:

$$\omega^{(t)} = SVM(X^{(t)}, y) \tag{17}$$

and the feature importance is calculated as:

$$S_i^{(4)} = \frac{1}{T}\sum\nolimits_{t=1}^{T}(\omega_i^{(t)})^2 \tag{18}$$

Since different feature selection algorithms generate scores with different numerical ranges, min-max normalization is applied:

$$\tilde{S}_i^{(m)} = \frac{S_i^{(m)} - \min_j(S_j^{(m)})}{\max_j(S_j^{(m)}) - \min_j(S_j^{(m)}) + \epsilon} \tag{19}$$

where ϵ is a small constant preventing division by zero.

The final feature importance score is obtained by weighted aggregation:

$$S_i^{agg} = \sum_{m=1}^{4}\omega_m \tilde{S}_i^{(m)} \tag{20}$$

where w_m denotes the weight assigned to the m-th feature selection method. The weights were empirically set as: $w_1 = 1.0, w_2 = 1.0, w_3 = 1.0, w_4 = 1.5$, where the larger weig
ht assigned to RFE reflects its wrapper-based evaluation capability through iterative model optimization.

After feature score aggregation, the top K_s discriminative mode-feature combinations are selected:

$$I_{sel} = TopK(S^{agg}, K_s) \tag{21}$$

Where K_s=100 and $I_{sel} = \{i_1, i_2, \ldots, i_{K_s}\}$ represents the selected feature index set.

Importantly, the selected indices correspond to mode-feature combinations rather than specific EEG channels. Therefore, the same feature index set is applied to every EEG channel, while the corresponding feature values remain channel-dependent.

For the n-th trial and c-th EEG channel, the final node feature vector is reconstructed as:

$$X_{node}^{(n,c)} = [x_{n,c,i_1}, x_{n,c,i_2}, \ldots, x_{n,c,i_{K_s}}] \in \mathbb{R}^{K_s} \tag{22}$$

where x_{n,c,i_j} denotes the value of the j-th selected mode-feature combination for channel c. Consequently, the final graph input feature tensor is represented as:

$$X_{GCN} = \mathbb{R}^{N\times C\times K_s} \tag{23}$$

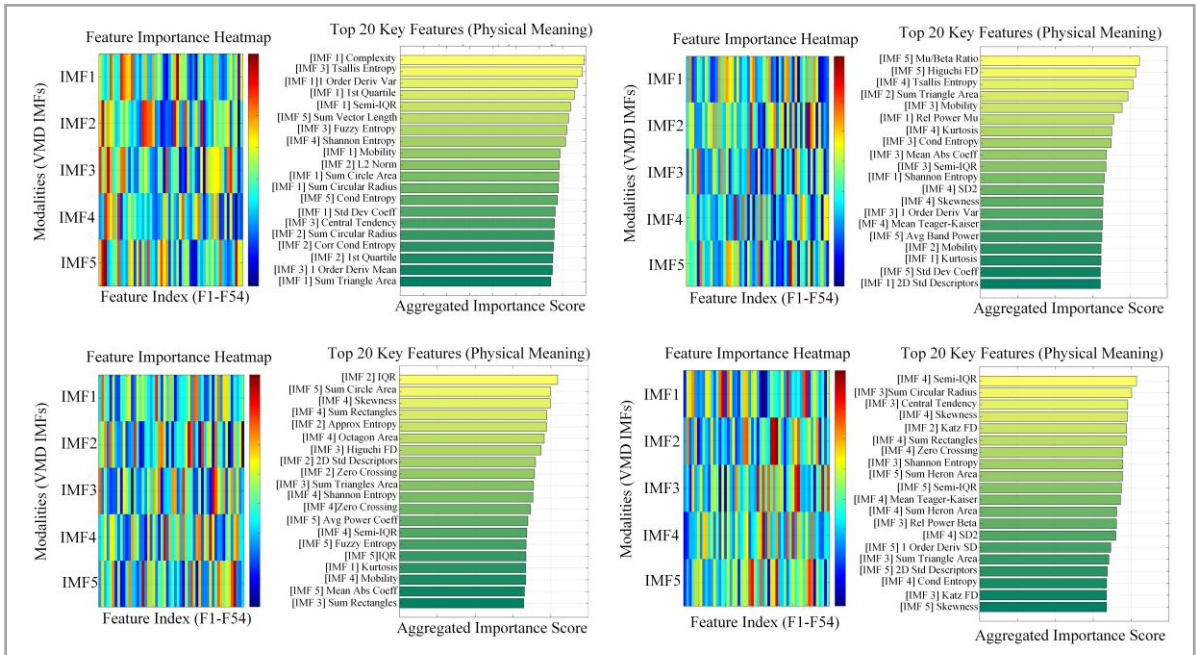


Figure 3. Unified Node Feature Selection Analysis and Top 20 Key Feature Distribution for GCN based on the MVMD-FS Framework.

where each EEG channel is treated as a graph node containing a unified K_s-dimensional feature representation.

This reconstruction strategy ensures consistent feature semantics among different EEG nodes while maintaining channel-specific neural information. Therefore, the graph convolutional network can effectively learn spatial dependencies among EEG channels based on comparable node embeddings. Meanwhile, computational complexity is effectively reduced through sample subsampling, candidate feature preselection, and parallel processing; furthermore, by reshaping the aggregated scores into the mode–feature space, feature importance is visualized to reveal the contribution distribution across multiple modes and feature domains, thereby enhancing the interpretability of the model.

As shown in Figure 3, the selected feature distributions exhibit clear inter-subject variability across subjects and experimental paradigms. To determine whether this variability reflects subject-dependent discriminative patterns rather than instability caused by the limited sample size, we further evaluated the robustness of the proposed feature selection strategy using repeated stratified cross-validation (Supplementary Material, Figure S1 and Table S2). The stability analysis demonstrated that the selected feature subsets were consistently more reproducible than random selection, indicating that the observed inter-subject variability is unlikely to arise solely from selection instability. Instead, it more plausibly reflects subject-dependent discriminative mode-feature patterns. Furthermore, the comparison between VR-MI and MI suggests that different experimental conditions emphasize different modal-feature combinations rather than fixed intrinsic mode identities. Overall, the proposed framework constructs stable and subject-specific node representations with consistent channel semantics, thereby facilitating subsequent graph-based decoding.

3.2.3. Graph Construction and GCN-Based Decoding Model

In this study, each EEG trial is modeled as a graph based on the underlying neurophysiological topology. Specifically, each sample is represented as a node-feature matrix $X \in R^{(C\times F)}$, where $C = 59$ denotes EEG channels (graph nodes) and $F = 100$ represents the selected node-wise feature dimension derived from MVMD decomposition and feature selection. In this study, to characterize

the dynamic functional connectivity of EEG signals across different trials, a trial-wise graph construction strategy is adopted. Specifically, for each EEG trial, the phase synchronization between channels is first computed on the 8–30 Hz bandpass-filtered signals, based on which a functional connectivity matrix is constructed to define the graph structure.Phase synchronization is quantified using the Phase Locking Value, which is calculated as follows:

$$PLV_{ij} = \left| \frac{1}{T} \sum_{t=1}^{T} e^{j(\phi_i(t) - \phi_j(t))} \right| \tag{24}$$

Where $\phi_i(t)$ and $\phi_j(t)$ denote the instantaneous phases of the *i*-th and *j*-th channels at time t, respectively, typically obtained via the Hilbert transform of the analytic signal, and *T* represents the number of time points. The PLV ranges from 0 to 1, reflecting the degree of phase synchronization between two brain regions.

Based on this, a symmetric functional connectivity matrix $PLV \in \mathbb{R}^{C \times C}$ is obtained, where each element represents the connection strength between a pair of channels. Considering the presence of noise and weak correlations in EEG signals, a sparsification strategy is applied to the PLV matrix to enhance the discriminative power of the graph structure and reduce redundant connections. For each trial, an adaptive threshold is determined according to the distribution of PLV values. By comparing different thresholding strategies (e.g., fixed thresholds and proportional thresholds), the upper quartile is ultimately selected as the sparsification threshold. Only strong connections are retained, and the adjacency matrix is defined as:

$$A_{ij} = \begin{cases} PLV_{ij}, & PLV_{ij} \geq \tau_q \\ 0, & \text{otherwise} \end{cases} \tag{25}$$

where τ_q denotes the upper quartile threshold of the PLV matrix for the current trial. This strategy preserves the most discriminative strong connections, effectively suppresses noisy links, and improves the stability of graph convolutional learning.

The graph structure is defined by a predefined adjacency matrix $A \in \mathbb{R}^{C \times C}$, which is further normalized as [47]:

$$\tilde{A} = D^{-\frac{1}{2}}(A + I)D^{-\frac{1}{2}} \tag{26}$$

to ensure numerical stability during graph convolution. Based on this graph representation, a hierarchical Graph Convolutional Network (GCN) is employed to model spatial dependencies across brain regions. Each graph convolution layer performs neighborhood feature aggregation and linear transformation as:

$$H^{(l+1)} = \sigma(\tilde{A} H^{(l)} W^{(l)}) \tag{27}$$

Where $H^{(l)}$ denotes node features at layer l, $W^{(l)}$ is the learnable weight matrix, and $\sigma(\cdot)$ is a nonlinear activation function. The first graph convolution layer projects node features from $C \times F$ to a higher-dimensional space while integrating first-order neighborhood information.

To further enhance discriminative capability and reduce redundancy, graph pooling is applied to perform node selection and hierarchical graph coarsening (e.g., 59→41). A second graph convolution layer is then applied on the reduced graph to capture higher-order topological interactions. Subsequent pooling further compresses the graph structure to obtain a compact high-level representation.

Finally, a global readout operation aggregates node-level features into a graph-level representation $h_{graph} \in \mathbb{R}^d$,which encodes the discriminative characteristics of the entire brain network. This representation is fed into a fully connected layer followed by a Softmax classifier to

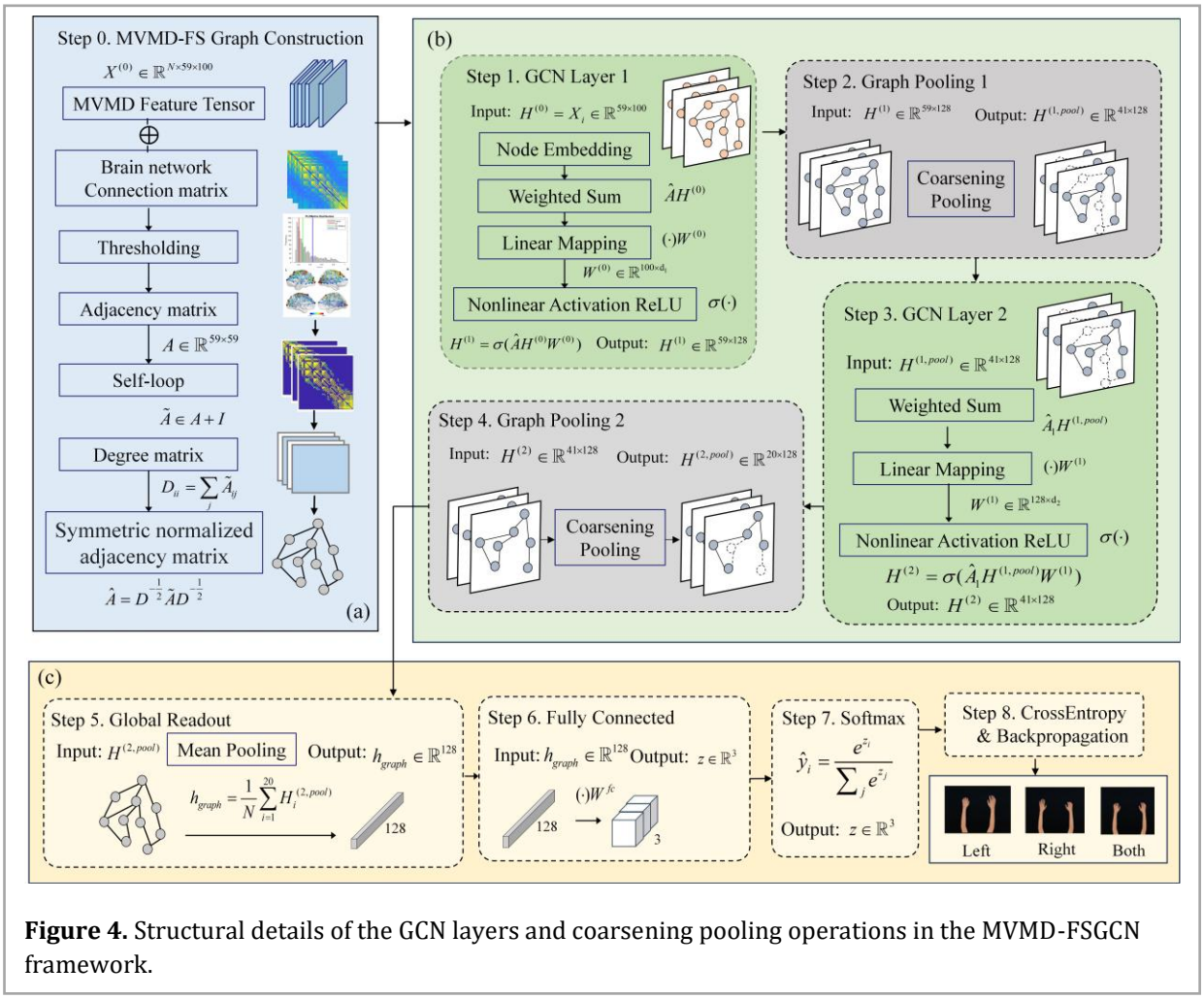


Figure 4. Structural details of the GCN layers and coarsening pooling operations in the MVMD-FSGCN framework.

produce class probabilities. The model is trained using cross-entropy loss and optimized via backpropagation.

This framework establishes a hierarchical mapping from node-level spectral-statistical features to graph-level discriminative representations, enabling unified modeling of spatial feature propagation, graph structure reduction, and global classification in non-Euclidean EEG data. Figure 4 provides a detailed schematic of the MVMD-FSGCN architecture, illustrating the specific computational flow from graph convolutional layers for spatial feature propagation to coarsening pooling operations for graph reduction. The specific architectural parameters and data flow dimensions for each layer of the proposed model, including the convolutional, pooling, and fully connected stages, are summarized in Table 2. The complete algorithmic logic of the MVMD-FSGCN framework is provided in Supplementary Algorithm S1.

Table 2. Feature Dimension Variations.

	Input	Convolutional layer 1	Graph Pooling 1	Convolutional layer 2	Graph Pooling 2	Readout	FC
Feature dimension	100	128	128	128	128	128	3
Number of nodes	59	59	41	41	20	1	\

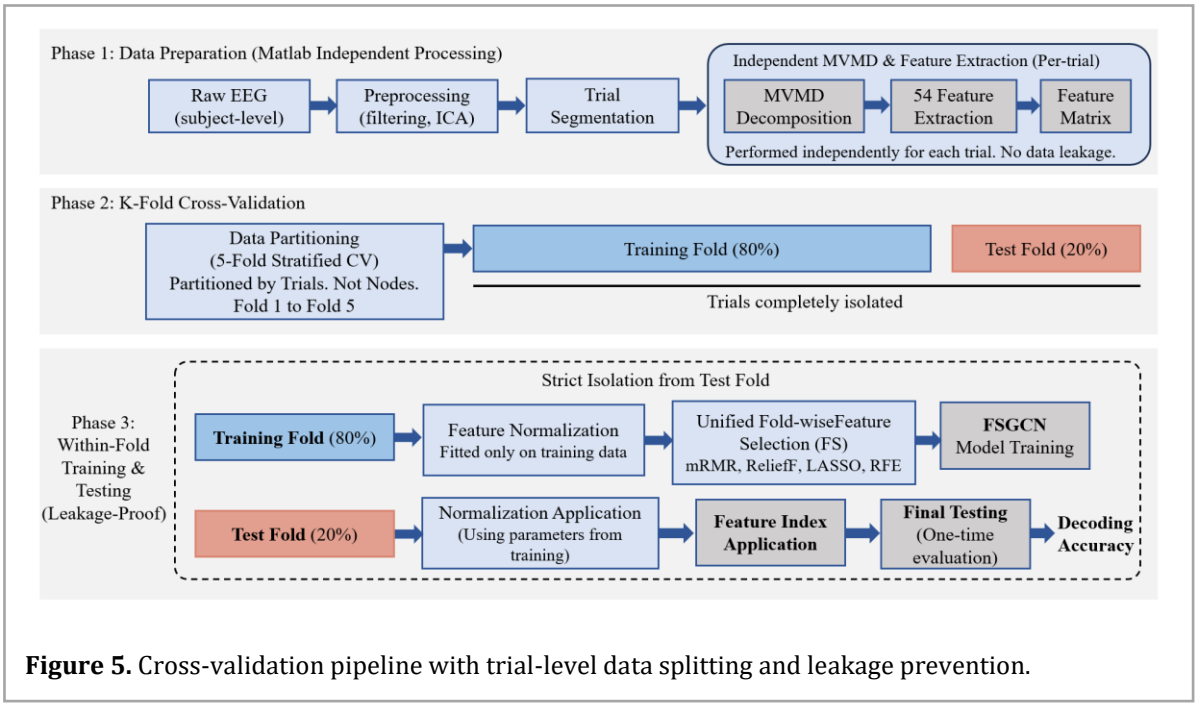


Figure 5. Cross-validation pipeline with trial-level data splitting and leakage prevention.

3.2.4. Data splitting and leakage prevention

To ensure the scientific rigor and generalizability of the proposed framework, a strict data isolation and evaluation protocol was implemented. Although feature extraction (via MVMD) and GCN-based classification are conducted as separate stages, the entire pipeline strictly adheres to the following leakage prevention principles: Trial-level Data Partitioning: The dataset was partitioned at the trial level using a stratified 5-fold cross-validation scheme. Importantly, the node-wise representation (i.e., channel-wise samples derived from each trial) was used only for feature organization, not for data splitting. All nodes (channels) belonging to the same trial were strictly assigned to the same fold. Therefore, no samples originating from the same trial appear in both training and testing sets, effectively preventing spatial-temporal leakage. Independent Feature Extraction: MVMD-based feature extraction was performed independently for each trial. The decomposition process and the computation of the 54 physical features relied solely on intra-trial information, without using any cross-trial statistics or global data distribution. This ensures that each trial is represented by fully self-contained features. Fold-specific Parameter Fitting: All normalization and scaling operations (e.g., Z-score standardization) were fitted exclusively on the training data within each fold. The estimated parameters (mean and standard deviation) were then applied to the corresponding test data. Under no circumstance was test data used to compute normalization parameters.

Internal Feature Selection: The multi-strategy feature selection methods were performed strictly within the training data of each fold. The test fold remained completely unseen during feature ranking and selection. The voting mechanism for feature aggregation was applied only within the training partitions of the current fold and did not involve any information from other folds or test data, thereby avoiding cross-fold information leakage.

One-time Final Evaluation: The test fold was used strictly once for final evaluation after model training and feature selection were fully completed. No model tuning, feature selection, or hyperparameter optimization was performed using the test data. This guarantees an unbiased estimation of the model's decoding performance. The overall data partitioning and validation strategy, including the measures to prevent information leakage between training and testing sets, are detailed in Figure 5.

4. Experiments and Results Analysis

4.1. Decoding Performance

Following the established MVMD-FSGCN framework, this section presents the performance evaluation and comparative analysis of the experimental data. Initially, 30 subjects were recruited for the experiment. However, after rigorous quality control, 2 subjects (S207 and S218) were excluded due to poor signal-to-noise ratio. The efficacy of the proposed model is highlighted through the analysis of the remaining 28 subjects. To ensure a fair and rigorous comparison, all models—including the proposed framework and the baseline methods—were evaluated using identical train/test partitions for each subject. This ensures that any performance differences are attributable to the model architectures rather than data splitting variability. To improve readability, Table 3 presents the detailed decoding performance of 10 example participants together with the group-level performance (Mean ± Std, N = 28). For each participant, the reported accuracy represents the

Table 3. Decoding Performance of Different Models on VR-MI and MI Data

Database	Subject_id	MVMD-FSGCN (%)	CSP+ MLP (%)	CSP+SVM (%)	EEGNet (%)	ATCNet (%)	EEG-Conformer (%)
VR-MI	S201	**72.73**	63.64	59.05	50.00	54.55	40.91
	S202	**70.37**	68.89	59.26	70.37	64.29	62.96
	S204	**83.33**	66.67	66.67	41.67	54.17	75.00
	S210	**86.67**	56.67	70.00	40.00	53.33	60.00
	S211	**83.33**	75.00	58.33	33.33	50.00	50.00
	S212	**75.00**	50.00	58.33	37.50	66.67	45.83
	S213	72.73	57.14	42.86	47.62	**76.19**	66.67
	S219	**72.73**	52.38	52.38	33.33	61.90	45.46
	S227	**87.50**	70.83	66.67	50.00	83.33	75.00
	S230	**83.33**	75.00	75.00	33.33	70.83	50.00
	Mean±Std (N=28)	**70.30 ±12.61**	55.05 ±14.64	54.71 ±14.65	42.32 ±11.12	57.85 ±10.88	56.19± 10.21
MI	S201	**55.65**	54.60	50.00	50.00	49.21	44.44
	S202	**58.33**	46.46	41.67	45.83	41.67	50.00
	S204	50.00	35.56	36.84	26.32	52.63	**70.00**
	S210	54.55	27.27	22.73	45.45	54.55	**72.73**
	S211	50.00	50.00	50.00	37.50	41.67	50.00
	S212	**83.33**	75.00	62.50	54.17	58.33	75.00
	S213	58.33	56.52	52.17	34.78	41.67	**66.67**
	S219	**45.45**	27.27	22.73	**45.45**	**45.45**	40.91
	S227	**79.17**	66.67	58.33	20.83	70.24	62.50
	S230	58.33	**66.67**	58.33	50.00	54.17	**66.67**
	Mean±Std (N=28)	**60.20 ±9.45**	50.74± 12.06	47.22± 13.20	39.15± 8.29	53.19 ± 7.89	54.47± 10.31

Note: Detailed metrics are shown for 10 example participants to improve readability, while the complete results for all 28 participants are provided in Supplementary Table S3. For each participant, the reported accuracy was first obtained by averaging the results over the five-fold cross-validation. The Mean ± Std (N = 28) rows therefore represent the mean accuracy and the inter-subject standard deviation calculated across the 28 evaluated participants, rather than the variability across cross-validation folds. The theoretical chance level for this three-class motor imagery task is 33.33%. VR-MI: Virtual Reality-based Action Observation and Motor Imagery; MI: Traditional Cue-based Motor Imagery.

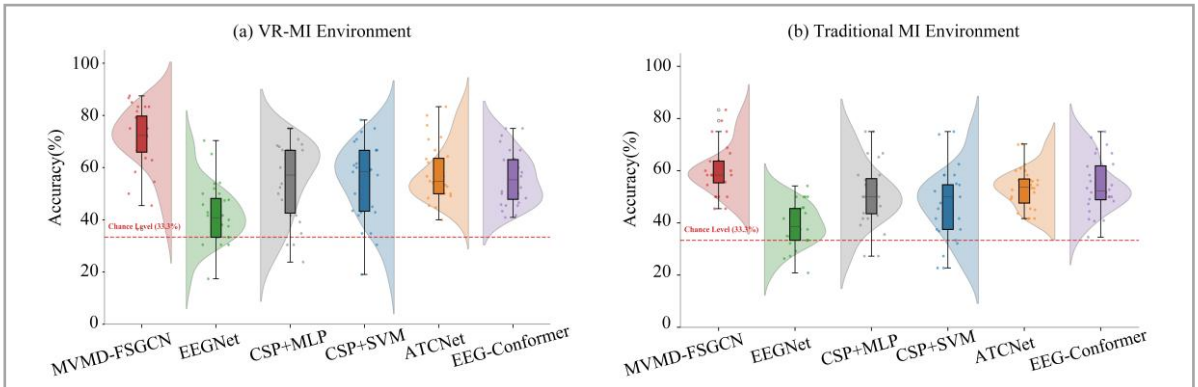


Figure 6. Individual-level decoding performance comparison across 28 subjects. Raincloud plots illustrate the multi-model classification accuracy distributions under (a) the VR-MI environment and (b) the traditional MI environment. Each plot dynamically combines data density profiles, box plots (representing the median and interquartile range), and subject-specific jittered data points. The horizontal red dashed line denotes the theoretical three-class chance level (33.33%).

average over the five-fold cross-validation, whereas the Mean ± Std values were calculated across the 28 evaluated participants. The complete participant-level results are provided in Supplementary Table S3, and the distributions of classification accuracies are illustrated using raincloud plots in Figure 6. The classification performance was evaluated across both the traditional cue-based MI and the VR-based AO+MI (VR-MI) datasets. To validate the robustness of the MVMD-FSGCN model, it was compared against several baseline methods: the classical shallow architectures including common spatial patterns (CSP) [48] combined with MLP and SVM, the standard deep-learning baseline EEGNet [49-50], and two state-of-the-art networks, namely ATCNet and EEG-Conformer. The comprehensive hyperparameter search strategies and architectural configurations for all implemented models are detailed in Supplementary Table S4. All experiments were conducted on a workstation equipped with an NVIDIA GeForce RTX 4090 GPU, ensuring efficient model training and inference. The EEG data preprocessing and feature extraction procedures, including MVMD decomposition and feature construction, were implemented in MATLAB R2021b (MathWorks, USA), while the model training and evaluation of the proposed FSGCN framework and comparative methods were performed in PyCharm 2025.1.1.1 using a Python-based deep learning environment.

As suggested by the statistical analyses summarized in Table 4, the proposed MVMD-FSGCN framework achieved a competitive performance advantage over both traditional machine learning and recent deep learning architectures across both experimental paradigms. Crucially, paired statistical comparisons across the 28 subjects indicated that the VR-based paradigm was associated with a statistically significant improvement in overall decoding accuracy compared to the traditional MI paradigm (mean difference = 10.09%, 95% CI = [3.76%, 16.42%], paired t-test: adjusted $p = 0.006$, Cohen's $d_z = 0.62$).

Furthermore, under the VR-MI condition, the performance of MVMD-FSGCN against all evaluated baselines appeared notably higher (all adjusted $p < 0.001$), demonstrating meaningful effect sizes over the classic EEGNet (mean difference = 27.97%, Cohen's dz = 1.99) as well as recent architectures including ATCNet (mean difference = 12.44%, Cohen's dz = 1.09) and EEG-Conformer (mean difference = 14.11%, Cohen's dz = 1.12).

Although EEGNet has achieved competitive performance on several public MI datasets, its performance in our study was relatively limited. One possible reason is the small subject-specific sample size. After artifact rejection, each subject contained only approximately 20–50 trials per class, and the effective training set became even smaller under five-fold cross-validation with validation splitting. Under such conditions, end-to-end models trained directly on raw EEG are more susceptible to overfitting and optimization instability, which may lead not only to lower average decoding accuracy but also to greater variability in performance across participants.

Table 4. Paired statistical comparisons of decoding accuracy across 28 subjects.

Comparison	Mean diff. (%)	95% CI	Test	Raw p	adjusted p	Cohen's d_z
VR-MI vs MI (MVMD-FSGCN)	10.09	[3.76, 16.42]	paired t-test	0.0029	0.006	0.62
MVMD-FSGCN vs CSP+MLP (VR-MI)	15.25	[11.44, 19.06]	paired t-test	< 0.001	< 0.001	1.55
MVMD-FSGCN vs CSP+SVM (VR-MI)	15.58	[11.49, 19.68]	paired t-test	< 0.001	< 0.001	1.48
MVMD-FSGCN vs EEGNet (VR-MI)	27.97	[22.52, 33.43]	paired t-test	< 0.001	< 0.001	1.99
MVMD-FSGCN vs ATCNet (VR-MI)	12.44	[8.00, 16.89]	paired t-test	< 0.001	< 0.001	1.09
MVMD-FSGCN vs EEG-Conformer (VR-MI)	14.11	[9.22, 19.00]	paired t-test	< 0.001	< 0.001	1.12
MVMD-FSGCN vs CSP+MLP (MI)	9.47	[6.39, 12.55]	paired t-test	< 0.001	< 0.001	1.19
MVMD-FSGCN vs CSP+SVM (MI)	12.98	[8.66, 17.30]	paired t-test	< 0.001	< 0.001	1.16
MVMD-FSGCN vs EEGNet (MI)	21.05	[16.62, 25.48]	paired t-test	< 0.001	< 0.001	1.84
MVMD-FSGCN vs ATCNet (MI)	7.01	[4.12, 9.90]	paired t-test	< 0.001	< 0.001	0.94
MVMD-FSGCN vs EEG-Conformer (MI)	5.74	[2.50, 10.31]	Wilcoxon	0.0099	0.010	0.58

Note: Statistical analyses were performed on decoding accuracies from 28 subjects. Mean differences were calculated as the performance difference between the first and second conditions in each comparison. The Shapiro–Wilk test was used to assess the normality of paired differences. Paired t-tests were used when the normality assumption was not rejected; otherwise, Wilcoxon signed-rank tests were used. Raw two-sided p-values and Holm-adjusted p-values are reported. The Holm correction was applied across the complete family of 11 paired comparisons shown in this table. For paired t-tests, the 95% CI represents the confidence interval of the mean paired difference. For Wilcoxon signed-rank tests, the 95% CI represents the Hodges–Lehmann confidence interval for the location shift. Cohen's dz was calculated as the standardized mean paired difference. A two-sided Holm-adjusted $p < 0.05$ was considered statistically significant.

In contrast, the proposed MVMD-FSGCN first performs signal decomposition and feature selection before graph learning, substantially reducing the dimensionality and improving the signal-to-noise ratio. Therefore, the graph classifier learns from compact discriminative representations instead of high-dimensional raw EEG, making it more suitable for limited-data scenarios.

4.2. Ablation Study

To quantify the contribution of each component in the proposed MVMD-FSGCN framework, ablation experiments were conducted by removing or replacing one module at a time. The evaluated factors include the signal decomposition strategy, feature selection, graph learning architecture,

Table 5. Ablation study of the main components of the proposed framework.

Task	Variant	FS	Classifier	ACC(%)	F1(%)	Kappa(%)
VR-MI	VMD variant	Multi-FS	Hierarchical GCN	66.65±14.77	64.66±18.88	45.14±24.33
	w/o FS	/	Hierarchical GCN	66.79±11.31	60.97±14.27	45.12±19.51
	w/o Graph	Multi-FS	MLP	54.02±16.72	52.85±17.20	30.99±15.03
			SVM	52.62±17.25	51.16±17.92	28.85±15.89
	w/o Hierarchical GCN	Multi-FS	Flat GCN	63.76±16.91	65.26±18.55	46.91±14.97
	Proposed	**Multi-FS**	**Hierarchical GCN**	70.30±12.61	65.78 ±15.09	53.10 ±18.58
MI	VMD variant	Multi-FS	Hierarchical GCN	59.13±12.35	52.97±12.87	32.44±16.66
	w/o FS	/	Hierarchical GCN	59.30±7.79	52.39±12.93	36.18±17.12
	w/o Graph	Multi-FS	MLP	40.81±9.55	38.76±10.23	31.08±14.41
			SVM	39.69±10.96	37.93±11.63	29.28±16.59
	w/o Hierarchical GCN	Multi-FS	Flat GCN	59.41±13.94	53.41±12.86	36.60±19.36
	Proposed	**Multi-FS**	**Hierarchical GCN**	60.20 ±9.45	53.57 ±13.87	37.21 ± 16.08

Note. Values are expressed as Mean ± Standard Deviation averaged across all 28 evaluated participants. Bold text indicates the optimal results achieved by the fully integrated proposed framework. "VMD variant" denotes the implementation using conventional channel-independent Variational Mode Decomposition instead of MVMD (K=5); "w/o FS" signifies the omission of the multi-strategy feature selection stage; "w/o Graph" isolates the impact of the GCN architecture by directly feeding the identical MVMD+FS features to classical flat classifiers; "w/o Hierarchical GCN" evaluates a standard flat GCN without the multi-scale graph pooling operation.

hierarchical pooling, graph construction, and sparsification. Results are summarized in Table 5, with the effect of the number of decomposition modes shown in Figure 7.

Replacing MVMD with the conventional VMD algorithm decreased the average accuracy on the VR-MI dataset from 70.30% to 66.65% (Table 5), indicating that joint multivariate decomposition better preserves inter-channel relationships than independent channel-wise processing. In the proposed framework, the decomposition mode number was fixed prior to the final evaluation based on preliminary methodological considerations and was kept unchanged throughout all cross-validation experiments. Figure 7 presents a parameter sensitivity analysis to evaluate the influence of different decomposition mode numbers rather than a hyperparameter optimization procedure. Specifically, five representative configurations (K = 1, 2, 3, 4, and 5) were evaluated. As shown in Figure 7, K = 5 achieved the highest average decoding accuracy while exhibiting the lowest inter-subject variability across both experimental paradigms, suggesting that finer multi-scale decomposition captures richer frequency-specific information while maintaining mode alignment across EEG channels. Larger values of K were not further investigated because increasing the number

Table 6. Ablation study of feature selection strategies.

Task	FS Strategy	ACC(%)	F1(%)	Kappa(%)
VR-MI	NoFS	66.79±11.31	60.97±14.27	45.12±19.51
	mRMR	64.79 ± 13.00	67.42 ± 18.19	45.60 ± 24.15
	ReliefF	63.98 ± 15.73	65.43 ± 17.76	43.66 ± 22.97
	LASSO	62.61 ± 15.22	65.78 ± 17.43	42.87 ± 22.85
	RFE	67.54 ± 12.85	66.81 ± 16.20	48.25 ± 20.10
	Multi-FS	70.30±12.61	65.78 ±15.09	53.10 ±18.58
MI	NoFS	59.30 ± 7.79	52.39 ± 12.93	36.18 ± 17.12
	mRMR	59.71 ± 13.67	53.87 ± 9.75	35.87 ± 9.75
	ReliefF	59.25 ± 14.39	52.96 ± 13.95	30.55 ± 17.20
	LASSO	55.49 ± 11.35	51.82 ± 12.60	36.68 ± 17.58
	RFE	59.86 ± 11.24	53.45 ± 11.50	36.10 ± 15.30
	Multi-FS	60.20 ±9.45	53.57 ±13.87	37.21 ± 16.08

Note: All variants used the same hierarchical GCN classifier and PLV-based graph construction. "NoFS" denotes the model trained with all extracted features without any feature selection. "mRMR", "ReliefF", "LASSO" and "RFE" denote variants using a single feature selection method, while "Multi-FS" represents the proposed weighted aggregation of all four methods. Results are reported as Mean ± Std across 28 subjects.

of decomposition modes substantially enlarges the feature space, thereby increasing the computational cost of feature extraction, feature selection, graph construction, and GCN training, while excessively large K may also introduce redundant decomposition modes.

Removing feature selection (w/o FS) reduced VR-MI accuracy from 70.30% to 66.79% (Table 5). Comparisons among individual methods (mRMR, ReliefF, LASSO,RFE) and the proposed weighted aggregation (Table 6) showed that the ensemble strategy generally achieved competitive performance, suggesting that different algorithms capture complementary discriminative information.

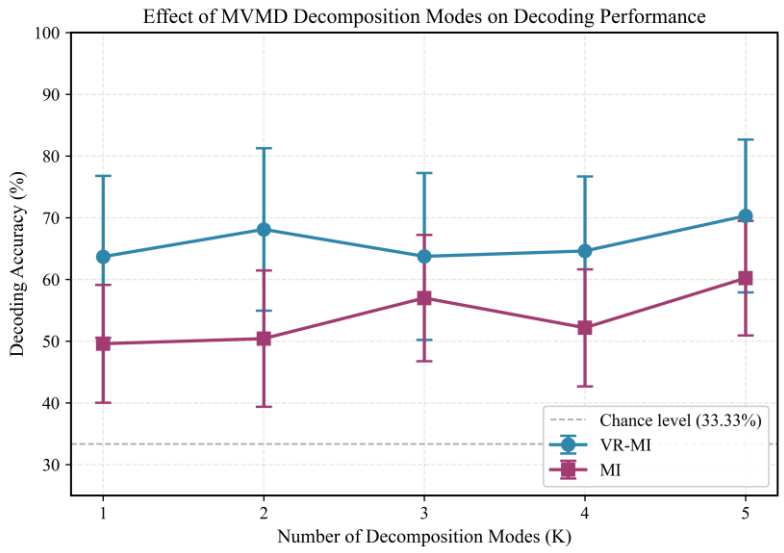


Figure 7. Parameter sensitivity analysis of the number of MVMD decomposition modes (K). The proposed framework was evaluated using fixed values of K (1–5), while all remaining parameters were kept unchanged. Error bars denote the standard deviation across all subjects, and the dashed line indicates the chance level (33.33%) for the three-class classification task.

Table 7. Ablation study of graph construction methods

Task	Graph Type	Graph Source	ACC (%)	F1 (%)	Kappa
VR-MI	Distance	Electrode geometry	64.11 ± 15.71	59.49 ± 10.06	50.02 ± 15.56
	Correlation	EEG correlation	64.72 ± 14.47	54.90 ± 8.07	42.33 ± 14.14
	kNN	Electrode neighborhood	63.40 ± 15.35	54.29 ± 9.37	43.08 ± 15.17
	PLV	**Functional connectivity**	70.30±12.61	65.78 ±15.09	53.10 ±18.58
MI	Distance	Electrode geometry	59.03 ± 10.67	53.55 ± 13.41	37.92 ± 17.57
	Correlation	EEG correlation	60.08 ± 10.82	56.21 ± 14.75	40.14 ± 19.78
	kNN	Electrode neighborhood	57.10 ± 10.98	53.79 ± 9.73	38.89 ± 12.66
	PLV	**Functional connectivity**	60.20 ±9.45	53.57 ±13.87	37.21 ± 16.08

Note: All variants used the same MVMD feature extraction, multi-strategy feature selection, and hierarchical GCN classifier. "Distance" denotes a graph constructed from Euclidean distances between electrode positions. "Correlation" denotes a graph based on Pearson correlation coefficients between EEG channel signals. "kNN" denotes a k-nearest-neighbor graph based on electrode spatial proximity. "PLV" denotes the proposed phase-locking value-based functional connectivity graph with upper-quartile sparsification. Results are reported as Mean ± Std across 28 subjects.

Table 8. Effect of PLV sparsification thresholds

Task	Threshold	ACC (%)	F1 (%)	Kappa
VR-MI	pct90	66.68 ± 15.12	56.05 ± 17.13	54.43 ± 21.78
	pct75	**70.30±12.61**	65.78 ±15.09	53.10 ±18.58
	pct50	66.19 ± 13.72	57.68 ± 19.78	55.04 ± 27.89
	Pct25	65.48 ± 13.78	56.42 ± 19.92	53.53 ± 27.86
	Full / pct0	65.84 ± 12.56	56.75 ± 19.26	53.74 ± 26.80
MI	pct90	55.83 ± 9.92	49.63 ± 9.33	34.26 ± 11.98
	pct75	**60.20 ±9.45**	53.57 ±13.87	37.21 ± 16.08
	pct50	57.39 ± 9.98	53.09 ± 14.30	36.24 ± 18.49
	Pct25	54.00 ± 10.00	51.16 ± 10.98	34.95 ± 12.80
	Full / pct0	57.24 ± 11.01	52.73 ± 12.88	36.60 ± 16.58

Note: All variants used the same MVMD feature extraction, multi-strategy feature selection, and hierarchical GCN classifier with PLV-based graph construction. The threshold "pctX" indicates that only edges with PLV values above the X-th percentile were retained. For example, "pct75" (the proposed setting) retains the top 25% of connections, while "pct90" retains only the top 10%. "Full / pct0" denotes the fully connected PLV graph without any sparsification. Results are reported as Mean ± Std across 28 subjects.

To isolate the contribution of the graph architecture from feature engineering, the same MVMD-derived features were fed to MLP and SVM classifiers. Both achieved substantially lower accuracy (54.02% and 52.62%, Table 5), confirming that the GCN architecture contributes beyond the input features alone. Replacing the hierarchical GCN with a flat GCN further reduced accuracy to 63.76%, indicating that hierarchical pooling provides additional benefit through multi-scale graph aggregation.

For VR-MI, the PLV-based functional connectivity graph achieved the highest accuracy and F1 among the graph constructions evaluated (Table 7), although the different metrics did not uniformly favour the same graph under MI. Among the sparsification thresholds examined (Table 8), pct75 achieved the highest accuracy and F1 in both conditions, whereas some alternative thresholds yielded slightly higher Kappa values.

Overall, the ablation experiments demonstrate that the performance improvement of the proposed MVMD-FSGCN framework results from the synergistic integration of multiple components rather than from any single module. MVMD provides discriminative multi-scale signal representations, the weighted multi-strategy feature selection enhances feature robustness, the PLV-based graph construction captures meaningful functional interactions among EEG channels, and the hierarchical GCN further exploits these graph structures through multi-scale representation learning. These complementary components may reduce the influence of subject-specific signal variations and contribute to more consistent decoding performance across participants, which is reflected by the relatively smaller inter-subject standard deviation observed in the VR-MI experiments.

5. Discussion

5.1. Decoding Performance

Table 9 summarizes the decoding performance of the same 10 illustrative participants presented in Table 3. For completeness, the detailed quantitative results across all 28 participants are provided in Supplementary Table S5.

5.2. VR-MI Brain Network Analysis

From a neuroanatomical perspective, the cerebral cortex is partitioned into the frontal, central, temporal, parietal, and occipital regions to provide a spatial framework for interpreting functional connectivity. EEG signals are band-pass filtered into Alpha (8–13 Hz) and Beta (13–30 Hz) bands. Task-related segments (0–4 s) corresponding to left-hand, right-hand, and both-hand MI are extracted based on event markers. For clarity, Figure 8 presents a representative example of the PLV-based functional brain network for the left-hand motor imagery task under the VR-MI paradigm in the alpha and beta frequency bands. The complete set of network visualizations for all tasks and paradigms is provided in the Supplementary Materials (Figure S3). Using the Hilbert transform, the analytical signal $x_a(t) = x(t) + j\hat{x}(t)$ is constructed to extract instantaneous phase $\phi(t)$ [51]. The PLV is calculated to quantify phase synchronization between channels i and j, following the procedure described in Section 3.2.3 (Eq. 24).

Table 9. Decoding performance comparison between VR-MI and traditional MI paradigms across ten representative subjects based on multiple evaluation metrics.

S_id	VR-MI					MI				
	acc	kappa	F1	precision	recall	acc	kappa	F1	precision	recall
S201	0.7273	0.5769	0.6833	0.8056	0.6944	0.5565	0.1667	0.3485	0.5565	0.4444
S202	0.7037	0.5556	0.6889	0.6854	0.7037	0.5833	0.5000	0.6722	0.5833	0.6667
S204	0.8333	0.7500	0.8222	0.8889	0.8333	0.5000	0.1935	0.3556	0.5000	0.4444
S210	0.8667	0.8000	0.8611	0.9048	0.8667	0.5455	0.2143	0.3905	0.5455	0.5000
S211	0.8333	0.7500	0.8222	0.8889	0.8333	0.5000	0.2500	0.3889	0.5000	0.3333
S212	0.7500	0.5625	0.7083	0.7083	0.7083	0.8333	0.6250	0.7368	0.8333	0.7500
S213	0.7273	0.5909	0.7182	0.7400	0.7100	0.5833	0.1818	0.3718	0.5833	0.4333
S219	0.7273	0.5823	0.7238	0.7238	0.7222	0.4545	0.1724	0.4404	0.4545	0.4464
S227	0.8750	0.8125	0.8721	0.8737	0.875	0.7917	0.7500	0.8320	0.7917	0.8333
S230	0.8333	0.7500	0.8320	0.8500	0.8333	0.5833	0.375	0.5582	0.6667	0.5833

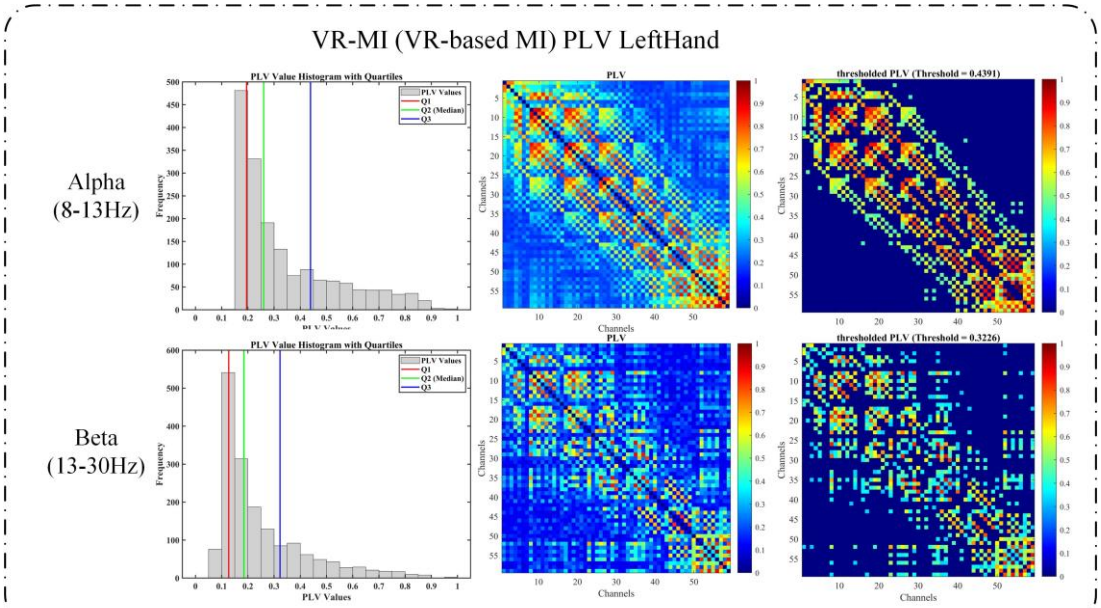


Figure 8. Representative PLV-based functional brain network patterns for the left-hand motor imagery task under the VR-MI paradigm in the alpha (8–13 Hz) and beta (13–30 Hz) frequency bands. For each frequency band, the left panel shows the distribution of PLV values, the middle panel presents the weighted connectivity matrix, and the right panel illustrates the corresponding thresholded (sparse) functional network. In the histogram plots, the red, green, and blue vertical lines indicate the lower quartile, median, and upper quartile of the PLV distribution, respectively, with the upper quartile used as the threshold for sparse network construction. The complete network visualizations for all tasks under both MI and VR-MI paradigms are provided in the Supplementary Materials (Figure S2).

BrainNetViewer [52] is utilized for network visualization. To ensure robustness across thresholds, a multi-threshold construction method based on sparsity (ranging from 0.10 to 0.40) is employed [53]. The Area Under the Curve (AUC) of the node degree (k_i) for key regions (C3 for right-hand, C4 for left-hand) is calculated as a stable metric of local integration. By using a quantile thresholding strategy to retain the strongest s% of connections, the weighted matrix is converted into a series of binary adjacency matrices $A^{(s)}$. At each sparsity level, the node degree of key regions in the contralateral motor cortex is calculated as an indicator of local network integration capacity.

$$k_i(s) = \sum_{j=1}^{N} A_{ij}^{(s)} \tag{28}$$

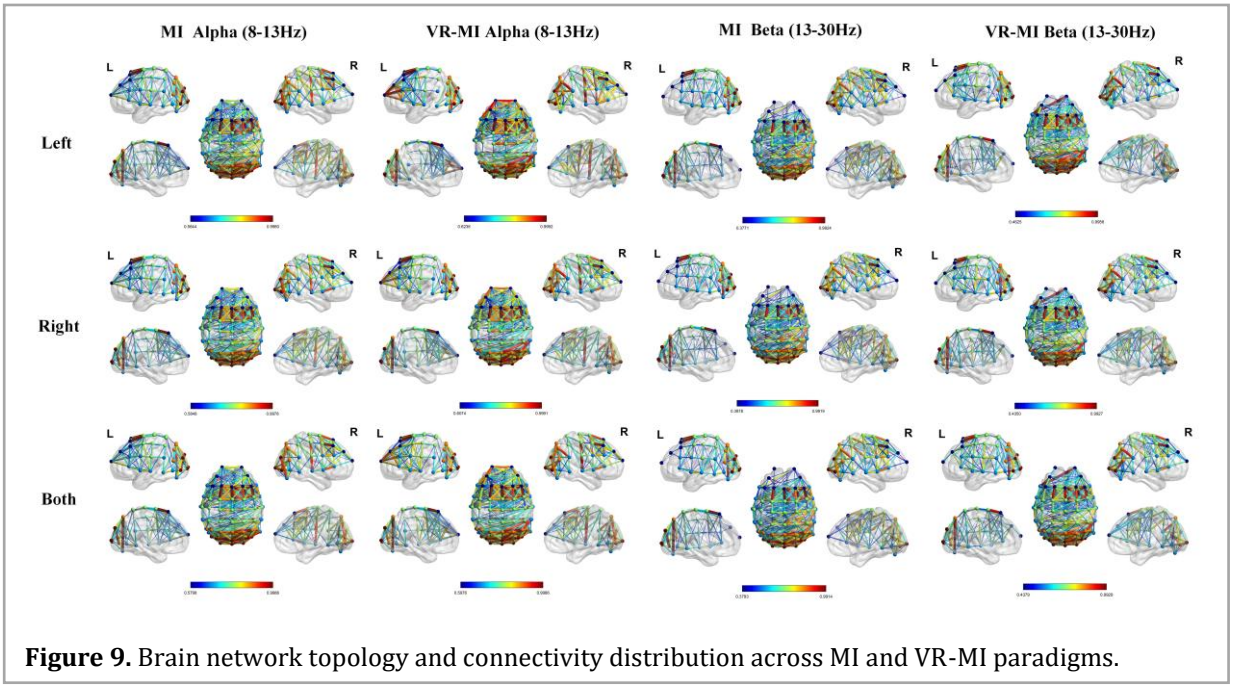


Figure 9. Brain network topology and connectivity distribution across MI and VR-MI paradigms.

The region of interest (ROI) is defined according to the contralateral control principle: the left-hand task corresponds to electrode C4, and the right-hand task corresponds to electrode C3 [54]. To obtain robust network indicators that are insensitive to the threshold, the node degree curve across different sparsity levels is integrated to calculate the AUC [55]:

$$AUC = \int_{S_{\min}}^{S_{\max}} k_i(s)ds \tag{29}$$

Using the anatomical framework of the cerebral cortex, the study visualized brain networks across five regions: Frontal, Central, Temporal, Parietal, and Occipital [56].

As depicted in Figure 9, Traditional MI networks showed sparse connections primarily localized in the sensorimotor area (C3/C4), whereas VR-MI showed broader interactions involving posterior areas (O1/O2 and P3/P4) and increased cross-regional connectivity in representative networks. These patterns suggest the involvement of additional visuomotor-related regions beyond the primary sensorimotor cortex during VR-based AO+MI. These topological diagrams are intended solely to provide a visual demonstration of functional patterns, whereas formal conclusions regarding network integration are based strictly on the group-level statistics (Table S6).

Group-level graph-theoretical analysis based on weighted PLV networks (Table S6) revealed frequency-dependent network alterations. After FDR correction, VR-MI significantly increased global efficiency and reduced characteristic path length in the Beta band (13–30 Hz) for both left- and right-hand tasks, indicating enhanced network integration. In contrast, Alpha-band changes did not reach statistical significance. Group-level analysis across 28 subjects evaluated the contralateral ROI connectivity strength (quantified by AUC) in the motor cortex between the two paradigms (Figure 10). Two-tailed Wilcoxon signed-rank tests were performed, with Holm-Bonferroni correction applied across frequency bands (Alpha/Beta) and task conditions (Left/Right hand). For the Beta band (13–30 Hz), the VR-based AO+MI paradigm showed a non-significant increasing trend in functional connectivity during left-hand MI tasks (raw p=0.0332, adjusted p_{adj}=0.1328), as well as a slight positive trend for right-hand tasks (raw p=0.0855, adjusted p_{adj}=0.1711).Within the Alpha band (8–13 Hz), a positive trend was similarly observed for left-hand tasks (raw p=0.0438, adjusted

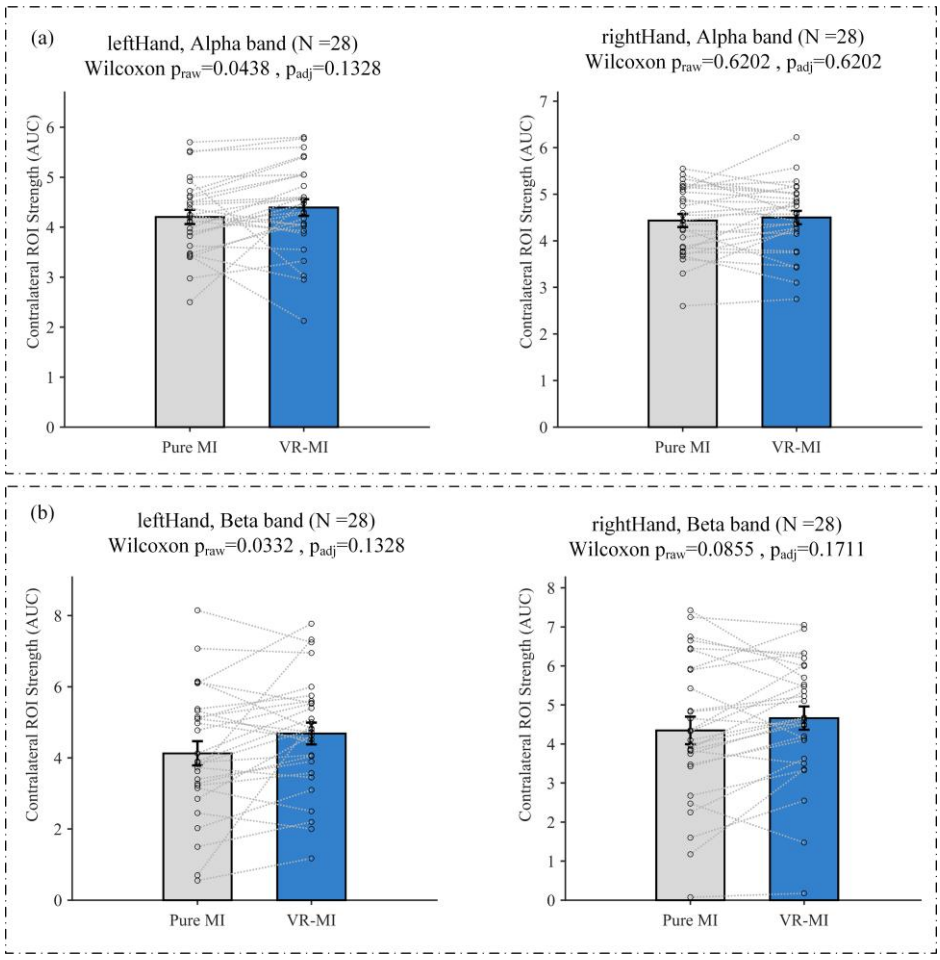


Figure 10. Statistical comparison of contralateral ROI connectivity strength (AUC) between Pure MI and VR-MI across Alpha (a) and Beta (b) bands for left and right hand tasks.

p_{adj}=0.1328), whereas right-hand tasks exhibited no noticeable differences (raw p=0.6202, adjusted p_{adj}=0.6202).

5.3. Limitations

A major limitation of this study is the confounding effect between VR-induced immersion and action observation (AO) cues. Our current setup cannot fully isolate whether the decoding enhancement stems from the immersive head-mounted display (HMD) or the virtual-hand movement cues, which are absent in traditional cue-based MI.

To address this, we conducted a preliminary pilot experiment using a screen-based AO+MI control condition with two participants (S227 and S230) who were available for additional data collection after the main study due to time constraints (see Supplementary Figure S3). Descriptive results (Supplementary Table S7) showed that while transitioning from abstract cues to screen-based virtual-hand feedback did not yield consistent improvements (S227: -5.10%; S230: -1.66%), the transition from screen to HMD-based VR presentation resulted in marked improvements for both participants(+13.43% and +26.66%, respectively). Importantly, this post-hoc observation serves strictly as a preliminary feasibility check and must not be used to establish an immersion effect or support the main statistical conclusions of this study. Future studies with larger sample sizes should employ a comprehensive control design—incorporating cue-based MI, screen-based AO+MI, VR-based AO+MI,—to strictly disentangle these factors.

Additionally, the present findings support subject-specific decoding under the stated five-fold cross-validation protocol, but they do not establish cross-subject or external-dataset generalisation. The limited per-subject trial counts and the practical burden of subject-specific calibration should therefore be considered when interpreting the results. Future work should evaluate the framework using cross-subject and independent-dataset protocols and, where appropriate, prospectively assess real-time performance in rehabilitation settings.

6. Conclusion

This study proposed a novel MVMD-FSGCN framework to investigate and enhance Motor Imagery decoding performance, with a particular focus on the impact of virtual reality-based motor imagery on neural representations. By integrating multivariate variational mode decomposition, multi-domain feature extraction, multi-strategy feature selection, and graph convolutional network-based brain network modeling, the framework establishes a unified pipeline for capturing the complex spectral–spatial characteristics of non-stationary EEG signals. Experimental results across 28 subjects demonstrate that the proposed method achieves superior decoding performance compared with traditional approaches (CSP+MLP, CSP+SVM) and deep learning baselines (EEGNet). Notably, the model attains a mean accuracy of 70.30% under VR-based AO+MI paradigm, significantly outperforming (Holm-adjusted $p = 0.006$, Cohen's $d_z = 0.62$) the traditional MI paradigm (60.20%), confirming the effectiveness of VR-based AO+MI paradigm in enhancing motor imagery decoding.

From a methodological standpoint, the MVMD-based decomposition provides a fine-grained, multi-scale representation of EEG signals, while the hybrid feature selection strategy effectively reduces spectral-temporal redundancy. The GCN-based modeling further captures the intrinsic topological structure of brain networks, enabling the learning of complex spatial dependencies. Crucially, this framework facilitates neurophysiological interpretability—a step toward addressing the 'black box' nature of deep learning in healthcare. Brain network analysis indicates that VR-based AO+MI paradigm fosters stronger functional connectivity and enhanced cross-regional integration, particularly within sensorimotor and parietal–occipital regions. These findings suggest that the combination of action observation and motor imagery facilitates neural decoding by promoting more effective neural coupling and multisensory integration.

CRediT authorship contribution statement

Kaiyue Du: Methodology, Visualization, Investigation, Writing-Original Draft, Writing-Reviewing, and Editing. Wenwen Chang: Writing-Review and Editing, Supervision, Visualization, Methodology, Resources, Funding acquisition. Weixuan Kong: Data curation, Software, Formal analysis, Investigation, Visualization. He Huang: Software, Formal analysis, Investigation, Visualization. Guanghui Yan: Supervision, Resources, Conceptualization, and Writing-Reviewing, Funding acquisition. Muhammad Tariq Sadiq: Conceptualization, Methodology, Formal analysis, Validation, Investigation, Visualization, Supervision, Writing – review & editing

Acknowledgements

This work was supported in part by the National Natural Science Foundation of China (Grant Nos. 62366028, W2421090, 62466032, and 82560281), the Gansu Provincial Major Science and Technology Project (Grant No. 23ZDFA012), the Gansu Provincial Natural Science Foundation (Grant No. 24JRRA256), the Gansu Provincial Science and Technology Talent Program Special Fund (Grant No. 26RCKA018), and the Gansu Provincial Education Digitalization Special Research Project (Grant No. JYSZH[2025]435).

References

[1] X.Y. Liu, W.L. Wang, M. Liu, M.Y. Chen, T. Pereira, D.Y. Doda, D. Ming, Recent applications of EEG-based brain-computer-interface in the medical field, Mil. Med. Res. 12 (2025) 14. https://doi.org/10.1186/s40779-025-00598-z.

[2] X. Wang, V. Liesaputra, Z. Liu, Y. Wang, Z. Huang, An in-depth survey on deep learning-based motor imagery electroencephalogram (EEG) classification. Artif. Intell. Med. 147 (2024) 102738. https://doi.org/10.1016/j.artmed.2023.102738.
[3] R. Lu, Z. Pang, T. Gao, Z. He, Y. Hu, J. Zhuang, Q. Zhang, Z. Gao, Multisensory BCI promotes motor recovery via high-order network-mediated interhemispheric integration in chronic stroke. BMC Med. 23 (2025) 380. https://doi.org/10.1186/s12916-025-04214-8.
[4] M.R.S. Bipul, M.A. Rahman, M.F. Hossain, Study on different brain activation rearrangement during cognitive workload from ERD/ERS and coherence analysis, Cogn. Neurodyn. 18 (2024) 1709–1732. https://doi.org/10.1007/s11571-023-10032-6.
[5] B. Blankertz, C. Sannelli, S. Halder, E.M. Hammer, A. Kübler, K.R. Müller, G. Curio, T. Dickhaus, Neurophysiological predictor of SMR-based BCI performance, NeuroImage 51 (2010) 1303–1309. https://doi.org/10.1016/j.neuroimage.2010.03.022.
[6] F. Lotte, L. Bougrain, A. Cichocki, M. Clerc, M. Congedo, A. Rakotomamonjy, F. Yger, A review of classification algorithms for EEG-based brain–computer interfaces: A 10 year update. J. Neural Eng. 15 (2018) 031005. https://doi.org/10.1088/1741-2552/aab2f2.
[7] B. Blankertz, R. Tomioka, S. Lemm, M. Kawanabe, K.R. Muller, Optimizing spatial filters for robust EEG single-trial analysis, IEEE Signal Process. Mag. 25 (2007) 41–56. https://doi.org/10.1109/MSP.2008.4408441.
[8] H.I. Suk, S.W. Lee, A novel Bayesian framework for discriminative feature extraction in brain-computer interfaces, IEEE Trans. Pattern Anal. Mach. Intell. 35 (2012) 286–299. https://doi.org/10.1109/TPAMI.2012.69.
[9] V.J. Lawhern, A.J. Solon, N.R. Waytowich, S.M. Gordon, C.P. Hung, B.J. Lance, EEGNet: A compact convolutional neural network for EEG-based brain–computer interfaces. J. Neural Eng. 15 (2018) 056013. https://doi.org/10.1088/1741-2552/aace8c.
[10] H. Altaheri, G. Muhammad, M. Alsulaiman, S.U. Amin, G.A. Altuwaijri, W. Abdul, M.A. Bencherif, M. Faisal, Deep learning techniques for classification of electroencephalogram (EEG) motor imagery (MI) signals: A review, Neural Comput. Appl. 35 (2023) 14681–14722. https://doi.org/10.1007/s00521-021-06352-5.
[11] Y. Song, Q. Zheng, B. Liu, X. Gao, EEG Conformer: Convolutional transformer for EEG decoding and visualization, IEEE Trans. Neural Syst. Rehabil. Eng. 31 (2022) 710–719. https://doi.org/10.1109/TNSRE.2022.3230250.
[12] H. Altaheri, G. Muhammad, M. Alsulaiman, Physics-informed attention temporal convolutional network for EEG-based motor imagery classification, IEEE Trans. Ind. Inform. 19 (2022) 2249–2258. https://doi.org/10.1109/TII.2022.3197419.
[13] Y. Ding, Y. Li, H. Sun, R. Liu, C. Tong, C. Liu, X. Zhou, C. Guan, EEG-Deformer: A dense convolutional transformer for brain-computer interfaces, IEEE J. Biomed. Health Inform. 29 (2024) 1909–1918. https://doi.org/10.1109/JBHI.2024.3504604.
[14] X. Ma, S. Qiu, C. Du, J. Xing, H. He, Improving EEG-based motor imagery classification via spatial and temporal recurrent neural networks, in: 2018 40th Annu. Int. Conf. IEEE Eng. Med. Biol. Soc. (EMBC), IEEE, 2018, pp. 1903–1906. https://doi.org/10.1109/EMBC.2018.8512591.
[15] N. Ur Rehman, H. Aftab, Multivariate variational mode decomposition, IEEE Trans. Signal Process. 67 (2019) 6039–6052. https://doi.org/10.1109/TSP.2019.2951223.
[16] M.T. Sadiq, X. Yu, Z. Yuan, M.Z. Aziz, N. ur Rehman, W. Ding, G. Xiao, Motor imagery BCI classification based on multivariate variational mode decomposition, IEEE Trans. Emerg. Top. Comput. Intell. 6 (2022) 1177–1189. https://doi.org/10.1109/TETCI.2022.3147030.
[17] J. Jian, D. Wu, J. Cao, F. Dong, J. Liu, D. Wang, S. Zhang, Grouped multivariate variational mode decomposition with application to EEG analysis, IEEE Trans. Biomed. Eng. 71 (2023) 1332–1344. https://doi.org/10.1109/TBME.2023.3334379.
[18] Q. Xue, Y. Song, H. Wu, Y. Cheng, H. Pan, Graph neural network based on brain inspired forward-forward mechanism for motor imagery classification in brain-computer interfaces. Front. Neurosci. 18 (2024) 1309594. https://doi.org/10.3389/fnins.2024.1309594.
[19] J. Leng, H. Li, W. Shi, L. Gao, C. Lv, C. Wang, F. Xu, Y. Zhang, T.P. Jung, Time-frequency-space EEG decoding model based on dense graph convolutional network for stroke, IEEE J. Biomed. Health Inform. 28 (2024) 5214–5226. https://doi.org/10.1109/JBHI.2024.3411646.
[20] Y. Ding, N. Robinson, C. Tong, Q. Zeng, C. Guan, LGGNet: Learning from local-global-graph representations for brain–computer interface, IEEE Trans. Neural Netw. Learn. Syst. 35 (2023) 9773–9786. https://doi.org/10.1109/TNNLS.2023.3236635.
[21] X. Tan, D. Wang, M. Xu, J. Chen, S. Wu, Efficient multi-view graph convolutional network with self-attention for multi-class motor imagery decoding. Bioengineering 11 (2024) 926. https://doi.org/10.3390/bioengineering11090926.
[22] M.M.N. Mannan, D.B. Palipana, K. Mulholland, E. Jurd, E.C. Lloyd, A.R. Quinn, C.B. Crossley, M.F. Rabbi, D.G. Lloyd, Y.D. Teng, C. Pizzolato, Virtual reality mediated brain-computer interface training improves sensorimotor neuromodulation in unimpaired and post spinal cord injury individuals. Sci. Rep. 16 (2026) 36431. https://doi.org/10.1038/s41598-026-36431-3.
[23] J.W. Choi, B.H. Kim, S. Huh, S. Jo, Observing actions through immersive virtual reality enhances motor imagery training, IEEE Trans. Neural Syst. Rehabil. Eng. 28 (2020) 1614–1622. https://doi.org/10.1109/TNSRE.2020.2998123.
[24] X. Xu, X. Fan, J. Dong, X. Zhang, Z. Song, W. Li, F. Pu, Event-related EEG desynchronization reveals enhanced motor imagery from the third person perspective by manipulating sense of body ownership with virtual reality for stroke patients, IEEE Trans. Neural Syst. Rehabil. Eng. 32 (2024) 1055–1067. https://doi.org/10.1109/TNSRE.2024.3365587.

[25] S. Cheng, Y. Liu, Y. Gao, Z. Dong, “As if it were my own hand”: Inducing the rubber hand illusion through virtual reality for motor imagery enhancement, IEEE Trans. Vis. Comput. Graph. 30 (2024) 7086–7096. https://doi.org/10.1109/TVCG.2024.3456147.
[26] M. Lin, J. Huang, J. Fu, Y. Sun, Q. Fang, A VR-based motor imagery training system with EMG-based real-time feedback for post-stroke rehabilitation, IEEE Trans. Neural Syst. Rehabil. Eng. 31 (2022) 1–10. https://doi.org/10.1109/TNSRE.2022.3210258.
[27] K. Lakshminarayanan, R. Shah, S.R. Daulat, V. Moodley, Y. Yao, D. Madathil, The effect of combining action observation in virtual reality with kinesthetic motor imagery on cortical activity. Front. Neurosci. 17 (2023) 1201865. https://doi.org/10.3389/fnins.2023.1201865.
[28] A. Gouret, A. Delaux, S. Le Bars, S. Chokron, Rewiring Attention: Virtual Reality and Brain–Computer Interfaces in the Rehabilitation of Unilateral Spatial Neglect. J. Clin. Med. 15 (2026) 1036. https://doi.org/10.3390/jcm15031036.
[29] R.C. Oldfield, The assessment and analysis of handedness: The Edinburgh inventory, Neuropsychologia 9 (1971) 97–113. https://doi.org/10.1016/0028-3932(71)90067-4.
[30] World Medical Association, World Medical Association Declaration of Helsinki: Ethical principles for medical research involving human subjects, JAMA 310 (2013) 2191–2194. https://doi.org/10.1001/jama.2013.281053.
[31] H.M. de Morree, C. Klein, S.M. Marcora, Cortical substrates of the effects of caffeine and time-on-task on perception of effort, J. Appl. Physiol. 117 (2014) 1514–1523. https://doi.org/10.1152/japplphysiol.00898.2013.
[32] G.H. Klem, The ten-twenty electrode system of the international federation, Electroencephalogr. Clin. Neurophysiol. Suppl. 52 (1999) 3–6.
[33] A. Delorme, S. Makeig, EEGLAB: An open source toolbox for analysis of single-trial EEG dynamics including independent component analysis, J. Neurosci. Methods 134 (2004) 9–21.
[34] Y. Jeon, C.S. Nam, Y.J. Kim, M.C. Whang, Event-related (De) synchronization (ERD/ERS) during motor imagery tasks: Implications for brain–computer interfaces, Int. J. Ind. Ergon. 41 (2011) 428–436. https://doi.org/10.1016/j.ergon.2011.03.005.
[35] D.J. McFarland, L.M. McCane, S.V. David, J.R. Wolpaw, Spatial filter selection for EEG-based communication, Electroencephalogr. Clin. Neurophysiol. 103 (1997) 386–394. https://doi.org/10.1016/S0013-4694(97)00022-2.
[36] T.P. Jung, S. Makeig, C. Humphries, T.W. Lee, M.J. Mckeown, V. Iragui, T.J. Sejnowski, Removing electroencephalographic artifacts by blind source separation, Psychophysiology 37 (2000) 163–178. https://doi.org/10.1111/1469-8986.3720163.
[37] Z. Wang, S. Li, X. Chen, D. Wu, Time–frequency transform based EEG data augmentation for brain–computer interfaces. Knowl.-Based Syst. 311 (2025) 113074. https://doi.org/10.1016/j.knosys.2025.113074.
[38] G. Kaushik, P. Gaur, R.R. Sharma, R.B. Pachori, EEG signal based seizure detection focused on Hjorth parameters from tunable-Q wavelet sub-bands. Biomed. Signal Process. Control 76 (2022) 103645. https://doi.org/10.1016/j.bspc.2022.103645.
[39] Y. Pei, J. Xu, Q. Chen, C. Wang, F. Yu, L. Zhang, W. Luo, DTP-Net: Learning to reconstruct EEG signals in time-frequency domain by multi-scale feature reuse, IEEE J. Biomed. Health Inform. 28 (2024) 2662–2673. https://doi.org/10.1109/JBHI.2024.3358917.
[40] W. Zeng, B. Su, C. Yuan, Y. Chen, Automatic detection of heart valve disorders using Teager–Kaiser energy operator, rational-dilation wavelet transform and convolutional neural networks with PCG signals, Artif. Intell. Rev. 56 (2023) 781–806. https://doi.org/10.1007/s10462-022-10184-7.
[41] J. Lerga, N. Saulig, V. Mozetič, Algorithm based on the short-term Rényi entropy and IF estimation for noisy EEG signals analysis, Comput. Biol. Med. 80 (2017) 1–13. https://doi.org/10.1016/j.compbiomed.2016.11.002.
[42] H.E. Abadi, M.K. Moridani, M. Mirzakhani, Mental arithmetic task detection using geometric features extraction of EEG signal based on machine learning, Bratisl. Med. J. 123 (2022) 405–412. https://doi.org/10.4149/BLL_2022_064.
[43] H. Peng, F. Long, C. Ding, Feature selection based on mutual information criteria of max-dependency, max-relevance, and min-redundancy, IEEE Trans. Pattern Anal. Mach. Intell. 27 (2005) 1226–1238. https://doi.org/10.1109/TPAMI.2005.159.
[44] I. Kononenko, E. Šimec, M. Robnik-Šikonja, Overcoming the myopia of inductive learning algorithms with RELIEFF, Appl. Intell. 7 (1997) 39–55. https://doi.org/10.1023/A:1008280620621.
[45] R. Tibshirani, Regression shrinkage and selection via the lasso, J. R. Stat. Soc. Ser. B (Methodol.) 58 (1996) 267–288. https://doi.org/10.1111/j.2517-6161.1996.tb02080.x.
[46] I. Guyon, J. Weston, S. Barnhill, V. Vapnik, Gene selection for cancer classification using support vector machines, Mach. Learn. 46 (2002) 389–422. https://doi.org/10.1023/A:1012487302797.
[47] Y. Hou, S. Jia, X. Lun, Z. Hao, Y. Shi, Y. Li, R. Zeng, J. Lv, GCNs-net: A graph convolutional neural network approach for decoding time-resolved EEG motor imagery signals, IEEE Trans. Neural Netw. Learn. Syst. 35 (2022) 7312–7323. https://doi.org/10.1109/TNNLS.2022.3202569.
[48] H. Ramoser, J. Muller-Gerking, G. Pfurtscheller, Optimal spatial filtering of single trial EEG during imagined hand movement, IEEE Trans. Rehabil. Eng. 8 (2000) 441–446. https://doi. org/10.1109/86.895946.
[49] D. Park, H. Park, S. Kim, S. Choo, S. Lee, C.S. Nam, J.Y. Jung, Spatio-temporal explanation of 3D-EEGNet for motor imagery EEG classification using permutation and saliency. IEEE Trans. Neural Syst. Rehabil. Eng. 31 (2023) 4504–4513. https://doi.org/10.1109/TNSRE.2023.3330922
[50] H. Song, Q. She, F. Fang, S. Liu, Y. Chen, Y. Zhang, Domain generalization through latent distribution exploration for motor imagery EEG classification. Neurocomputing 614 (2025) 128889. https://doi.org/10.1016/j.neucom.2024.128889.
[51] J.P. Lachaux, E. Rodriguez, J. Martinerie, F.J. Varela, Measuring phase synchrony in brain signals, Hum. Brain Mapp. 8 (1999) 194–208. https://doi.org/10.1002/(SICI)1097-0193(1999)8:4<194::AID-HBM4>3.0.CO;2-C.

[52] M. Xia, J. Wang, Y. He, BrainNet Viewer: A network visualization tool for human brain connectomics. PLOS ONE 8 (2013) e68910. https://doi.org/10.1371/journal.pone.0068910.
[53] C. Bordier, C. Nicolini, A. Bifone, Graph analysis and modularity of brain functional connectivity networks: Searching for the optimal threshold. Front. Neurosci. 11 (2017) 441. https://doi.org/10.3389/fnins.2017.00441.
[54] M. Okamoto, H. Dan, K. Sakamoto, K. Takeo, K. Shimizu, S. Kohno, I. Oda, S. Isobe, T. Suzuki, K. Kohyama, I. Dan, Three-dimensional probabilistic anatomical cranio-cerebral correlation via the international 10–20 system oriented for transcranial functional brain mapping, NeuroImage 21 (2004) 99–111. https://doi.org/10.1016/j.neuroimage.2003.08.026.
[55] M. Drakesmith, K. Caeyenberghs, A. Dutt, G. Lewis, A.S. David, D.K. Jones, Overcoming the effects of false positives and threshold bias in graph theoretical analyses of neuroimaging data, NeuroImage 118 (2015) 313–333. https://doi.org/10.1016/j.neuroimage.2015.05.011.
[56] L. Koessler, L. Maillard, A. Benhadid, J.P. Vignal, J. Felblinger, H. Vespignani, M. Braun, Automated cortical projection of EEG sensors: Anatomical correlation via the international 10–10 system, NeuroImage 46 (2009) 64–72. https://doi.org/10.1016/j.neuroimage.2009.02.006.